

SIMULATIONS OF DAMPED LYMAN-ALPHA AND LYMAN LIMIT ABSORBERS IN DIFFERENT COSMOLOGIES: IMPLICATIONS FOR STRUCTURE FORMATION AT HIGH REDSHIFT

Jeffrey P. Gardner¹, Neal Katz², Lars Hernquist^{3,4}, David H. Weinberg⁵

E-mail: gardner@astro.washington.edu, nsk@kaka.phast.umass.edu, lars@cfa.harvard.edu, dhw@astronomy.ohio-state.edu

ABSTRACT

We use hydrodynamic cosmological simulations to study damped Ly α (DLA) and Lyman limit (LL) absorption at redshifts $z = 2 - 4$ in five variants of the cold dark matter scenario: COBE-normalized (CCDM), cluster-normalized (SCDM), and tilted (TCDM) $\Omega = 1$ models, and open (OCDM) and flat (LCDM) $\Omega_0 = 0.4$ models. The simulations resolve the formation of dense concentrations of neutral gas in halos with circular velocity $v_c \geq v_{c,res} \approx 125 \text{ km s}^{-1}$ for $\Omega = 1$ and 80 km s^{-1} for $\Omega_0 = 0.4$, at $z = 2$. We find a clear relation between HI column density and projected distance to the center of the nearest galaxy, with DLA absorption usually confined to galactocentric radii less than $10 - 15 \text{ kpc}$ and LL absorption arising out to projected separations of 30 kpc or more. Considering only absorption in the resolved halos, all five models fall short of reproducing the observed amount of DLA and LL absorption at these redshifts, sometimes by large factors (especially for LL absorption and for TCDM). If any of these cosmological models is correct, then a substantial fraction of DLA and LL absorption must arise in halos with $v_c \leq 100 \text{ km s}^{-1}$; this conclusion seems qualitatively consistent with imaging studies of DLA systems but requires that the large velocity spreads in associated metal-line absorption be boosted by non-equilibrium dynamics. We also find evidence for non-equilibrium effects on the geometric cross section for high column density absorption. Individual absorbers are smaller in more massive halos because gas sinks deeper into the potential wells, but more massive halos tend to have multiple gas concentrations and therefore have larger absorption cross sections on average. We estimate the amount of absorption in halos with $v_c < v_{c,res}$ using a numerically calibrated analytic procedure similar to that employed in our earlier work, but improvements to the details of the method lead

¹University of Washington, Department of Astronomy, Seattle, WA 98195

²University of Massachusetts, Department of Physics and Astronomy, Amherst, MA 01003-4525

³University of California, Lick Observatory, Santa Cruz, CA 95064

⁴Department of Astronomy, Harvard University, Cambridge, MA 02138

⁵Ohio State University, Department of Astronomy, Columbus, OH 43210

to significantly higher predictions for absorption by unresolved halos. The addition of low mass halo absorption makes all five models consistent with the observed DLA and LL abundance at the $\sim 2\sigma$ level or better, given the observational and theoretical uncertainties. More robust tests of cosmological models against the observed amount of high column density absorption will require simulations of representative volumes that resolve the $v_c \sim 50 - 100 \text{ km s}^{-1}$ halos where most of the absorption is predicted to occur. Our analytically corrected numerical results raise the interesting possibility that LL absorption is closely akin to DLA absorption, arising in less massive halos or at larger galactocentric radii but not caused by processes acting on a radically different mass scale.

Subject headings: quasars: absorption lines, galaxies: formation, large scale structure of the Universe

1. Introduction

Systems producing absorption in the spectra of distant quasars offer an excellent probe of the early Universe. At high redshifts, they easily outnumber other observed tracers of cosmic structure, including both normal and active galaxies. The interpretation of low column density quasar absorption systems has undergone somewhat of a revolution during the past several years, with the recognition that they may consist of gas aggregating into mildly nonlinear structures analogous in their dynamical structure to today's galaxy superclusters (Cen et al. 1994; Petitjean et al. 1995; Zhang et al. 1995, 1997; Hernquist et al. 1996; Miralda-Escudé et al. 1996; Bi & Davidsen 1997; Hui, Gnedin, & Zhang 1997). However, damped Ly α (DLA) absorbers, with neutral hydrogen column densities $N_{\text{HI}} \geq 10^{20.3} \text{ cm}^{-2}$, are usually thought to be associated with the dense interstellar gas of high-redshift galaxies, based on several lines of circumstantial evidence: similarity between the column densities of damped systems and the column densities through typical spiral disks today, rough agreement between the total mass of atomic hydrogen in damped absorbers at $z \sim 3$ and the total mass of stars today (Wolfe & Prochaska 1998), measurements of radial extents $\gtrsim 10h^{-1} \text{ kpc}$ in two DLA systems (Briggs et al. 1989; Wolfe et al. 1993), and direct imaging of a number of DLA hosts from ground based and HST observations (Djorgovski et al. 1996; Fontana et al. 1996; Moller & Warren 1998; Le Brun et al. 1997). The nature of Lyman limit (LL) absorbers, with $N_{\text{HI}} \geq 10^{17.2} \text{ cm}^{-2}$, is less well understood, though most models associate them with the outer regions of galaxies (e.g., Mo & Miralda-Escudé 1996).

Analytic studies based on the Press-Schechter (1974) formalism suggested that the abundance of DLA systems might be a strong test of cosmological models, potentially ruling out those models with little power on galaxy scales at $z = 3$ (Kauffmann & Charlot 1994; Mo & Miralda-Escudé 1994). The most sophisticated of these calculations, that of Kauffmann (1996), implied that the “standard” cold dark matter model (SCDM, with $\Omega = 1$, $h \equiv H_0/100 \text{ km s}^{-1} \text{ Mpc}^{-1} = 0.5$,

and a power spectrum normalization $\sigma_8 \approx 0.7$) could account for the observed abundance of high-redshift DLA systems, with about 30% of the absorption at $z = 2.5$ occurring in galaxies with halo circular velocities $v_c > 100 \text{ km s}^{-1}$. Katz et al. (1996, hereafter KWHM) presented the first predictions of the amount of DLA and LL absorption based on 3-dimensional hydrodynamic simulations, concluding that these simulations of the SCDM model came within a factor of two of matching the observed DLA abundance but fell nearly an order of magnitude short of reproducing observed LL absorption. Ma et al. (1997) “calibrated” DLA estimates from collisionless N-body simulations against the KWHM SCDM simulations, then applied this calibration to N-body simulations of cold+hot dark matter (CHDM) models. They concluded that the CHDM scenario failed to reproduce the observed DLA abundance even with a neutrino fraction as low as $\Omega_\nu = 0.2$, strengthening the earlier, analytic arguments, which focused on CHDM with $\Omega_\nu = 0.3$.

The shortcoming of the KWHM calculation was that it could not include the contribution from DLA and LL systems below its resolution limit, corresponding to a halo circular velocity $v_c \sim 100 \text{ km s}^{-1}$. In Gardner et al. (1997a; GKHW hereafter), we remedied this shortcoming by combining the KWHM results with high resolution simulations of individual, low mass objects similar to those of Quinn, Katz, & Efstathiou (1996; QKE hereafter). We used these simulations to obtain a relation between absorption cross-section α and halo circular velocity v_c , which we combined with the Press-Schechter halo abundance to compute the total amount of DLA and LL absorption in the SCDM model. The correction for previously unresolved halos increased the predicted absorption by about a factor of two, bringing the predicted DLA abundance into good agreement with observations but leaving the predicted number of LL systems substantially below the observed number.

In Gardner et al. (1997b; GKWH hereafter), we applied the $\alpha(v_c)$ relation derived for SCDM to other cosmological models, obtaining more general predictions for DLA and LL absorption under the assumption that the relation between halo v_c and gas absorption cross-section was independent of cosmological parameters. We have since carried out simulations of several variants of the inflation+CDM scenario (see, e.g., Katz, Hernquist & Weinberg 1999), and in this paper we improve upon the GKWH results by using these simulations to predict DLA and LL absorption in these models. We thereby obtain more robust, numerical predictions for absorption in halos above the simulation resolution limits, $v_c \sim 80 - 125 \text{ km s}^{-1}$ (at $z = 2$). We continue to use a Press-Schechter based extrapolation to compute the contribution of smaller halos to DLA and LL statistics, employing an improved methodology that significantly changes the GKHW predictions for absorption by low mass systems. We also revisit an issue explored by KWHM for the SCDM model, the predicted distribution of projected separations between DLA and LL systems and high-redshift galaxies.

The nature of the galaxies that host DLA systems has been a controversial topic for many years. Two competing hypotheses have defined the poles of the debate: the idea that most DLA systems are large, rotating gas disks (e.g., Schiano, Wolfe, & Chang 1990), and the idea that a large fraction of DLA absorption arises in dwarf galaxies (e.g., Tyson 1988). The strongest empirical

argument for the dwarf hypothesis is that some imaging studies reveal small galaxies near the line of sight but no clear candidates for large galaxies producing the absorption (e.g., Fontana et al. 1996; Le Brun et al. 1997; Moller & Warren 1998). The recent study of two DLA systems at $z = 0.091$ and $z = 0.221$ by Rao & Turnshek (1998) places especially stringent upper limits on the luminosities of the host galaxies. The strongest argument for the rotating disk hypothesis is the analysis of metal-line kinematics in DLA systems by Prochaska & Wolfe (1997, 1998), who consider a variety of simplified models for the velocity structure of the absorbers and find that only a population of cold, rotating disks with typical circular velocities $v_c \gtrsim 200 \text{ km s}^{-1}$ can account for the observed distribution of velocity spreads and for the high frequency of “lopsided” kinematic profiles. However, hierarchical models of galaxy formation predict that such massive disks should be rare at $z \sim 3$. In an important paper, Haehnelt, Steinmetz, & Rauch (1998) showed that hydrodynamic simulations of high-redshift galaxies could account for the lopsided kinematic profiles and large velocity spreads found by Prochaska & Wolfe (1997, 1998) even with halo circular velocities substantially below 200 km s^{-1} , because of large scale asymmetries and departures from dynamical equilibrium (see also Ledoux et al. 1998). This result makes the $\sim 100 \text{ km s}^{-1}$ median halo circular velocities found by Kauffmann (1996) and GKHW for the SCDM model potentially compatible with the observed metal-line kinematics.

Our present simulations do not have enough resolution for us to repeat the Haehnelt et al. (1998) analysis; we hope to do so with future simulations in order to carry out a statistical comparison between results from a randomly chosen cosmological volume and the Prochaska & Wolfe (1997, 1998) data. However, we can already extend the GKHW analysis to other cosmological models, predicting the fraction of DLA absorption arising in halos of different circular velocities. The high resolution simulations of localized regions by QKE and GKHW indicate that halos with v_c as low as 35 km s^{-1} can host damped absorbers, so our direct numerical results, with resolution limits $v_c \sim 80 - 125 \text{ km s}^{-1}$, yield only lower limits to the total amount of DLA and LL absorption. We apply two improved variants of the GKHW procedure to correct for absorption by unresolved halos, with the difference between them serving as an estimate of the systematic uncertainty associated with the correction. Section 2 describes the simulations and our analysis methods. Section 3 presents our analysis of the DLA and LL systems resolved by the simulations. Section 4 describes and applies our procedures for computing the contribution from unresolved halos. We discuss the implications of our results in §5 and summarize our conclusions in §6.

2. Simulations and Methods

2.1. The Simulations

Our simulations follow the same general prescription as in GKHW, where a periodic cube whose edges measure $11.11h^{-1}\text{Mpc}$ in comoving units is drawn randomly from a CDM universe and evolved to a redshift $z = 2$. The parameters of each model are detailed in Table 1. The

quantity n is the index of the inflationary fluctuation spectrum, with $n = 1$ corresponding to scale-invariant fluctuations. These are the same simulations presented by Katz et al. (1999), who studied the clustering properties of the galaxies. We will often refer to the three $\Omega = 1$ models (SCDM, CCDM, TCDM) collectively as the “critical” models and the two $\Omega_0 = 0.4$ models (OCDM, LCDM) as the “subcritical” models.

The simulations employ 64^3 gas and 64^3 dark matter particles, with a gravitational softening length of $5h^{-1}$ comoving kpc ($3h^{-1}$ comoving kpc equivalent Plummer softening, $1h^{-1}$ physical kpc at $z = 2$). The particle masses are $1.5 \times 10^8 M_\odot$ and $2.8 \times 10^9 M_\odot$ for the gas and dark matter, respectively, in the critical models and $6.7 \times 10^7 M_\odot$ and $8.3 \times 10^8 M_\odot$ in the subcritical models.

Detailed descriptions of the simulation code and the radiation physics can be found in Hernquist & Katz (1989) and Katz, Weinberg, & Hernquist (1996; hereafter KWH), and we only summarize the techniques here. We perform our simulations using TreeSPH (Hernquist & Katz 1989), a code that unites smoothed particle hydrodynamics (SPH; Lucy 1977; Gingold & Monaghan 1977) with the hierarchical tree method for computing gravitational forces (Barnes & Hut 1986; Hernquist 1987). Dark matter, stars, and gas are all represented by particles; collisionless material is influenced only by gravity, while gas is subject to gravitational forces, pressure gradients, and shocks. We include the effects of radiative cooling, assuming primordial abundances, and Compton cooling. Ionization and heat input from a UV radiation background are incorporated in the simulation. We adopt the UV background spectrum of Haardt & Madau (1996), but reduce it in intensity by a factor of two at all redshifts so that the mean Ly α forest flux decrement is close to the observed value given our assumed baryon density (Croft et al. 1997). We apply small further adjustments to the background intensity during the analysis stage to precisely match the Press, Rybicki, & Schneider (1993) measurements of the mean decrement (see Croft et al. 1997 for further discussion of this procedure). We use a simple prescription to turn cold, dense gas into collisionless “star” particles. The prescription and its computational implementation are described in detail by KWH. Details of the numerical parameters can be found in Katz et al. (1999).

Name	σ_8	Ω_0	Ω_Λ	h	Ω_b	n	M_{res}
SCDM	0.7	1	0	0.5	0.05	1	$1.9 \times 10^{11} M_\odot$
CCDM	1.2	1	0	0.5	0.05	1	$1.9 \times 10^{11} M_\odot$
TCDM	0.54	1	0	0.5	0.05	0.8	$1.9 \times 10^{11} M_\odot$
OCDM	0.75	0.4	0	0.65	0.03	1	$5.8 \times 10^{10} M_\odot$
LCDM	0.8	0.4	0.6	0.65	0.03	0.93	$5.8 \times 10^{10} M_\odot$

Table 1: Model parameters.

2.2. Halo and Absorber Identification

From the simulation outputs at $z = 4$, 3, and 2, we identify dark matter halos and the individual concentrations of cold, collapsed gas that they contain. We identify the halos by applying a friends-of-friends algorithm to the combined distribution of dark matter and SPH particles, with a linking length equal to the mean interparticle separation on an isodensity contour of an isothermal sphere with an enclosed average overdensity of $\delta_{vir} \equiv \rho_{vir}/\bar{\rho} - 1$ equal to the virial overdensity. In an isothermal sphere, the local density at the virial radius is simply one third the virial overdensity, which we calculate using the prescription found in Kitayama & Suto (1996). In the critical density models, the friends-of-friends linking parameter is $b = 0.00318$ of the box edge length, or $64 \times b = 0.204$ of the initial interparticle grid spacing (note, however, that gas and dark matter particles start on two offset 64^3 grids).

To detect discrete regions of collapsed gas capable of producing Lyman limit and damped Ly α absorption, we apply the algorithm of Stadel et al. (2000; see also KWH and <http://www-hpcc.astro.washington.edu/tools/SKID>) to the distribution of cold gas and star particles. SKID identifies gravitationally bound groups of particles that are associated with a common density maximum. Gas particles are only considered as potential members of a SKID group if they have smoothed overdensity $\rho_g/\bar{\rho}_g - 1 > \delta_{vir}$ and temperature $T < 30,000$ K, and we discard groups with fewer than four members (we will apply a more stringent resolution cut below). All of the gas concentrations found by this method reside within a larger friends of friends halo, even at $z = 4$. We match each absorber with its parent halo and discard halos that contain no absorbers.

For each of the halos that contain a cold gas concentration, we determine the radius of the sphere centered on the most tightly bound particle within which the average overdensity is equal to δ_{vir} . We characterize halo masses and circular velocities by their values at this radius, which we define to be the virial radius. This method of quantifying the properties of halos in the simulations corresponds to the spirit of the Press-Schechter approximation, which is based on the spherical collapse model. We find that the mass distribution of halos in the simulations is best fit using the Press-Schechter form with a Gaussian filter and a threshold density contrast for collapse of $\delta_c = 1.69$. Many workers instead use a top hat filter, with $M_f = (4\pi/3)\rho_0 R_f^3$ (cf. Ma 1996; Ma & Bertschinger 1994; Mo & Miralda-Escudé 1994; Mo et al. 1996), or a Gaussian filter with a modified relation between filter radius and associated mass, $M_f = 6\pi^2\rho_0 R_f^3$ (Lacey & Cole 1994), with similar values for δ_c . However, these studies use the halo masses returned by the friends of friends algorithm itself, and if we were to do this we would also find that top hat or modified Gaussian filters provide good fits to the mass function for $\delta_c \approx 1.7$. The combination $\delta_c = 1.69$, Gaussian filter, and $M_f = (2\pi)^{3/2}\rho_0 R_f^3$ works much better for our definition of halo mass using the spherical overdensity technique. Including or excluding the “absorberless” halos in our mass function does not change the results above our resolution cutoff (explained below), since nearly all halos above our cutoff contain at least one absorber.

We calculate the HI column densities for the halos by enclosing each halo within a sphere

centered on the most tightly bound gas particle and of sufficient size to contain all the gas particles that might contribute to high column density absorption within the halo. We project the gas distribution within this sphere onto a uniform grid of cell size 5.43 comoving kpc, equal to the highest resolution achieved anywhere in the simulation, using the same spline kernel interpolation employed by the TreeSPH code for the hydrodynamics. Following KWHM, we calculate an initial HI column density for each grid point assuming that the gas is optically thin, then apply a self-shielding correction to yield a true HI column density (see KWHM for details). For each halo we compute the projected area over which it produces damped absorption, with $N_{\text{HI}} > 10^{20.3} \text{ cm}^{-2}$, and Lyman limit absorption, with $N_{\text{HI}} > 10^{17.2} \text{ cm}^{-2}$. For simplicity, we project all halos from a single direction, although we obtain a similar fit of absorption area to circular velocity (see below) if we project randomly in the x , y , and z directions or average the projections in x , y , and z . Projecting a rectangular prism instead of a sphere yields the same results. To test for convergence, we reprojected several halos at 2 and 4 times smaller grid spacings and found that the cross section for DLA and LL absorption changed by less than 1% in the majority of cases and at most 2.5%.

2.3. Numerical Resolution Considerations

Current hydrodynamic simulations lack the dynamic range needed to model simultaneously the full mass range of objects that can contribute to DLA and LL absorption. The simulations of QKE and GKHW show that halos with circular velocities as low as 35 km s^{-1} can host DLA absorbers, while photoionized gas is unable to collapse and cool in smaller halos. However, if we adopted a particle mass low enough to resolve 35 km s^{-1} halos, then our simulation volume would be too small to include a representative sample of more massive halos.

In our analysis of the simulation results, we find that halos consisting of at least 60 dark matter particles nearly always (more than 98% of the time) contain a cold, dense gas concentration. Below this threshold, however, a substantial fraction of halos have no cold gas concentration. Furthermore, in our bootstrap analysis of the variance in the relation between halo v_c and absorption cross-section, described in §4.1 below, we find much larger scatter about the mean relation for halos with fewer than 60 dark matter particles than for halos with more than 60 dark matter particles. Both of these results lead us to adopt $M_{\text{res}} = 60(m_{\text{dark}} + m_{\text{SPH}})$ as an estimate of the limiting mass below which we cannot accurately compute the amount of absorption in a simulated halo. We will eventually be able to test this estimate by comparing our current simulations to simulations with higher mass resolution; a preliminary investigation along these lines supports our choice of 60 particles as a reasonable one. The 60 particle criterion is more conservative than the 34 particle criterion that we adopted in GKHW, and this change will affect our predictions for the total amount of absorption in §4.2 below.

In the critical density models, the mass resolution limit is $M_{\text{res}} = 1.9 \times 10^{11} M_{\odot}$, corresponding to a circular velocity at the virial radius of $v_{c,\text{res}} = 125, 140$, and 160 km s^{-1} at $z = 2, 3$, and 4 ,

respectively. In the subcritical models, $M_{res} = 5.8 \times 10^{10} M_{\odot}$, corresponding to $v_{c,res} = 80, 89$, and 100 km s^{-1} at $z = 2, 3, 4$ (see GKHW eq. 3 for the relation between v_c , M , and z). For our statistical analyses of the simulation results below, we always eliminate absorbers in halos whose total mass (dark matter plus baryons, with the spherical overdensity mass definition given above) is $M < M_{res}$. Our quoted results apply only to halos above the resolution limit. In §4, we attempt to compute the contribution of halos with $M < M_{res}$ to the total amount of DLA and LL absorption by combining the Press-Schechter approximation with our numerical results.

We assume throughout our subsequent analysis and discussion that our results for absorption in halos with $M > M_{res}$ are only minimally influenced by the residual effects of finite numerical resolution. This need not be the case; for instance, real absorption systems could have substructure that produces large fluctuations in HI column density on scales far below our resolution limit. In this scenario, the total amount of neutral gas in absorption systems would not be very different from our predictions, except to the extent that clumping shifts gas above or below the DLA/LL column density thresholds, but the distribution of column densities above the thresholds could be quite different. This issue will be difficult to address by direct numerical simulation alone because of the large range of scales involved. However, good agreement between predicted and observed column density distributions would support the contention that the absorbers do not have a great deal of substructure on scales below the simulation resolution limits. KWHM find good agreement between the predicted and observed shape of the column density distribution in the DLA regime, but a compelling case along these lines will require simulations that do resolve the full mass range of objects responsible for damped absorption, and such simulations are probably still several years away.

3. Simulation Results

Figures 1 and 2 show the incidence of DLA and LL absorption in our five cosmological models: $n(z)$ is the mean number of absorbers intercepted per unit redshift above the DLA (Fig. 1) or LL (Fig. 2) column density threshold. The numerical results for halos above the mass resolution limit M_{res} are shown at $z = 2, 3$, and 4 . Observational results for DLA absorption are taken from Storrie-Lombardi, Irwin, & McMahon (1996a; cf. also Wolfe et al. 1995) and for LL absorption from Storrie-Lombardi et al. (1994). When comparing the subcritical models to the critical models, note that the subcritical models have lower M_{res} and therefore sample the distribution of absorbers down to a lower mass cutoff, boosting the $n(z)$ prediction relative to that of the critical models. Taken directly from the simulations and from halos only above M_{res} , the values in these plots are hard lower limits to the predicted $n(z)$. The limiting circular velocities $v_{c,res}$ are well below the value $v_c \sim 200 \text{ km s}^{-1}$ inferred by Prochaska & Wolfe (1997, 1998) for typical DLA circular velocities based on a rotating disk model for metal-line kinematics, and even so the predicted number of DLA absorbers is usually a factor of two or more below the observed value. We conclude that if the inflationary CDM models considered here are even approximately correct,

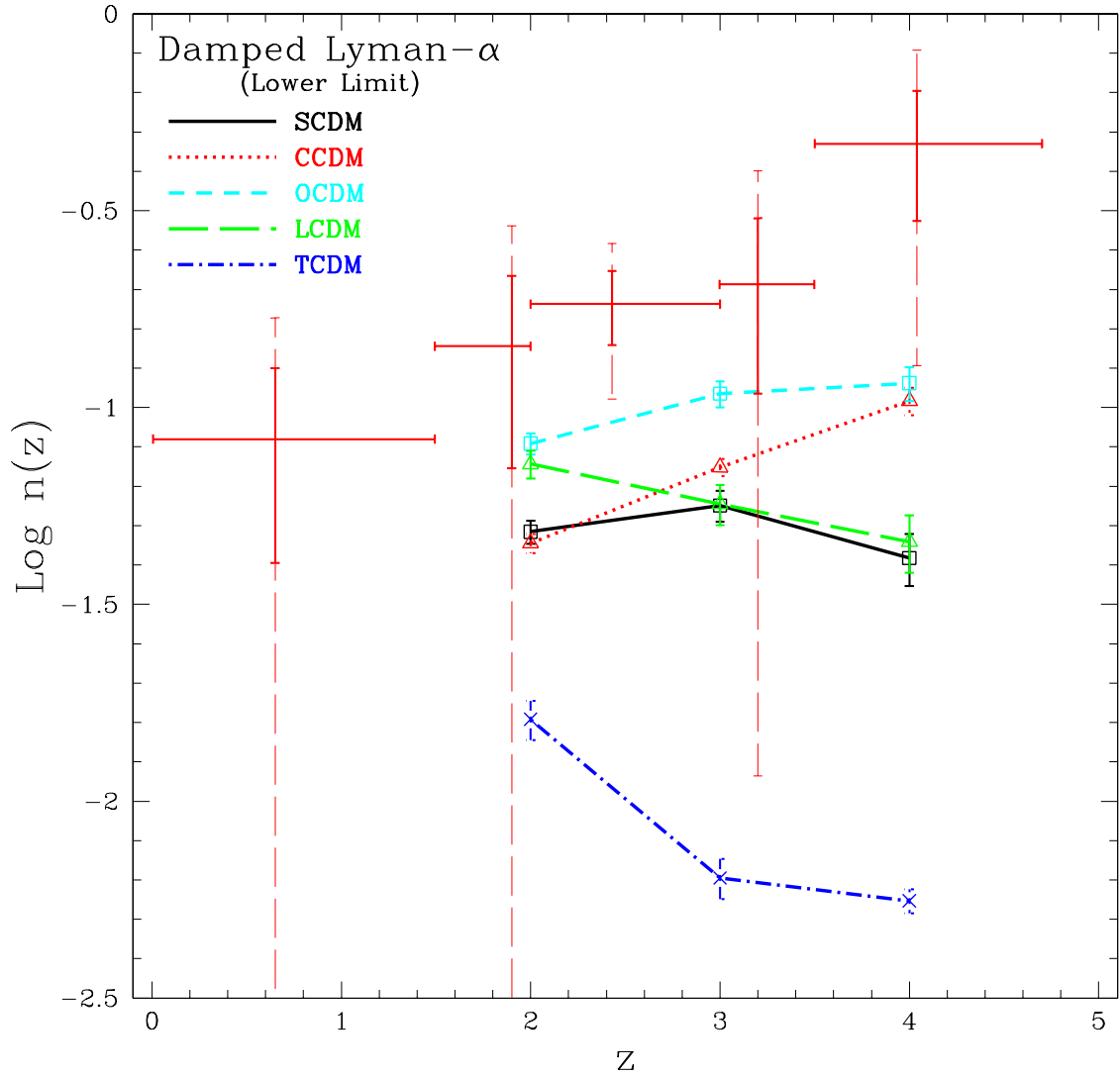


Fig. 1.— The incidence of DLA absorption in simulations of the five cosmological models listed in Table 1; $n(z)$ is the number of systems with $N_{\text{HI}} \geq 10^{20.3} \text{ cm}^{-2}$ intercepted per unit redshift. Simulation results are computed only for absorption in halos with mass above the mass resolution limits M_{res} listed in Table 1. Observational data from Storrie-Lombardi et al. (1996a), shown with 1σ (solid) and 2σ (dashed) error bars, indicate DLA absorption by systems of all masses. The deficiency of absorption in the models may be explained partly or entirely by the contribution from halos below the simulations' resolution limits (see §4).

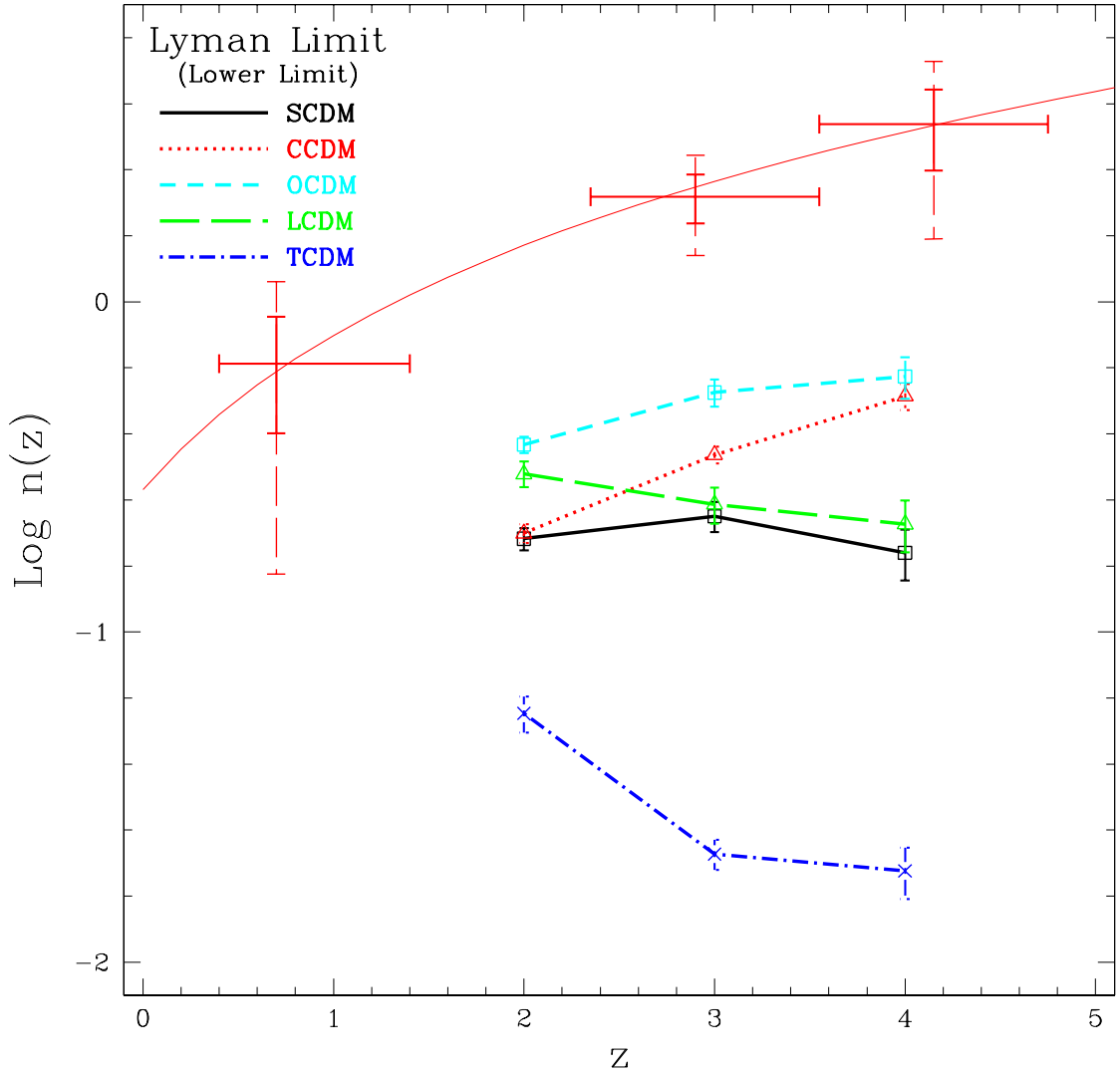


Fig. 2.— The incidence $n(z)$ of LL absorption associated with halos above the simulation resolution limits. The format is similar to Fig. 1, but the threshold column density is now $N_{\text{HI}} \geq 10^{17.2} \text{ cm}^{-2}$. The upper error crosses represent the Lyman limit data of Storrie-Lombardi et al. (1994), with 1σ and 2σ abundance errors. The smooth curve shows their fitted power law. Observational values include systems of all masses.

then the asymmetries and large velocity spreads found by Prochaska & Wolfe must be a result of complex geometry and non-equilibrium dynamics, as proposed by Haehnelt et al. (1998).

Figure 3 shows the distribution of impact parameters D_{proj} , in physical units, between high column density absorbers and the centers of neighboring galaxies. Specifically, the contour level represents the percentage of lines of sight of a given N_{HI} for which the closest simulated galaxy, in projection, lies within a projected distance D_{proj} . Note that in this figure and in further figures we represent distance in kpc and not h^{-1} kpc. Nearly all of the high column density systems in our simulations are associated with a galaxy, with the highest column density systems sampling the innermost regions of the galaxy and the lower column density systems occurring at larger impact parameters. At $z = 2$, nearly all DLA systems lie within 15-20 kpc of a galaxy center, and nearly all LL systems lie within 30 kpc. At higher redshifts, the most likely impact parameter increases, which could indicate a physical contraction of DLA systems as they age or could alternatively reflect the higher neutral fraction associated with a given overdensity at higher redshift (similar to the interpretation of evolution of the low column density forest given by Hernquist et al. 1996 and Davé et al. 1999).

Figure 4 shows the fraction of critical density in cold collapsed gas, Ω_{ccg} (solid line), and the fraction of the critical density in stars, Ω_{\star} (dotted line), as a function of redshift in the various cosmological models. In subcritical models, we define $\Omega_x(z) \equiv \rho_x(z) \times (1+z)^{-3}/\rho_c(z=0)$, i.e., Ω_x represents the comoving density of component x relative to the critical density at $z = 0$. We obtain Ω_{ccg} by integrating the column density distribution $f(N_{\text{HI}})$ for all of the halos in the simulation. Error crosses show the values derived by Storrie-Lombardi, McMahon, & Irwin (1996b) from a sample of DLA systems. The largest observed column density for DLA systems in the Storrie-Lombardi et al. (1996ab) sample is $10^{21.8} \text{ cm}^{-2}$, probably because higher column density systems are too rare to have been detected. For a more direct comparison to the data, we therefore compute an “observational” value, Ω_{obs} , for which we only count gas along lines of sight with $N_{\text{HI}} \leq 10^{21.8} \text{ cm}^{-2}$. The contribution to Ω_{ccg} from higher column density systems is generally small, but it is significant in the SCDM model. In all cases, we include only gas in halos with $v_c \geq v_{c,\text{res}}$.

For all the models in Figure 4, Ω_{\star} increases steadily as the Universe evolves. However, Ω_{ccg} remains constant to within a factor of two from redshift 4 down to redshift 2, indicating that additional gas cools and collapses to replace the gas that is turned into stars. Gas reaches higher densities in the the SCDM and CCDM models, leading to a larger difference between Ω_{ccg} and Ω_{obs} . In nearly all cases, our “observed” cold gas densities Ω_{obs} fall at least a factor of two below the observational data of Storrie-Lombardi et al. (1996b), which could themselves be underestimates of the true cosmological values of Ω_{ccg} if dust extinction is important (Pei & Fall 1995). If any of these models are to be viable, a substantial fraction of the high redshift HI must reside in systems below our resolution limit, an issue to which we turn in §4.

To obtain the simulation values of Ω_{ccg} in Figure 4, we had to alter the procedure described

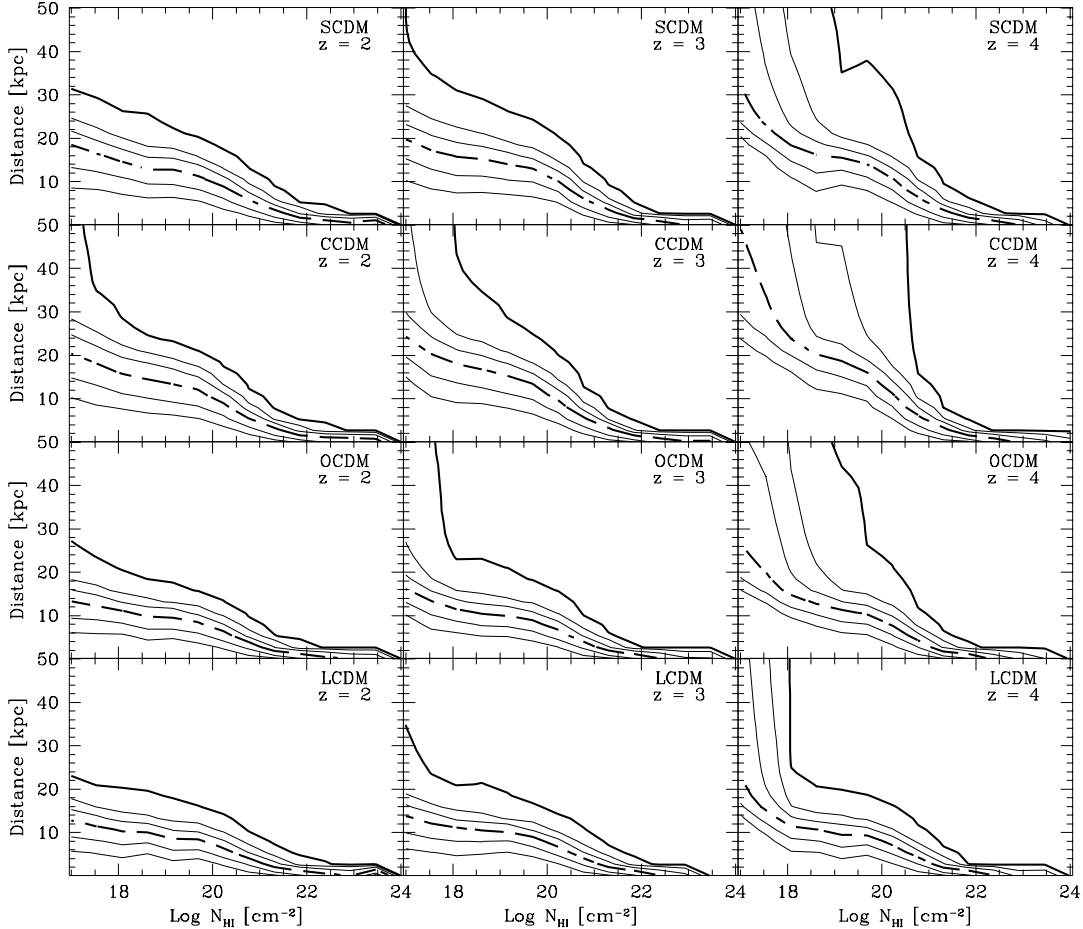


Fig. 3.— The distribution of impact parameters D_{proj} from high column density lines of sight to neighboring galaxies. The x -axis denotes the HI column density along the line of sight. The y -axis is the projected distance D_{proj} (in physical kpc) to the galaxy in the simulation volume that lies closest (in projection) to the line of sight. The contours indicate the percentage of lines of sight containing an absorber of HI column density N_{HI} that have a galaxy whose center is within D_{proj} . The thin contour levels are 10%, 25%, 75% and 90% with the dashed thick line denoting 50% and the solid thick line 99%. To construct the contours of the plot, lines of sight in the simulations were sorted into bins $\Delta N_{\text{HI}} = 0.5$ dex and $\Delta D_{\text{proj}} = 2.5$ kpc wide.

in §2.2 for computing HI column densities. While our standard grid spacing of 5.43 comoving kpc is sufficient to resolve objects with HI columns of $10^{20.3} \text{ cm}^{-2}$ and lower, a finer mesh is required to resolve the cold dense knots of gas at higher column densities, which contribute significantly to the Ω_{ccg} integral. As described in KWHM, we generate the initial HI map assuming complete transparency, then use the mass, HI mass fraction, and temperature of each grid cell to correct the HI column density for its ability to shield itself from the surrounding radiation. Typically, a high column density grid cell contains some regions where the hydrogen should be partly ionized and some where it should be completely neutral owing to self-shielding effects. At the standard resolution of 5.43 comoving kpc, our procedure may average the contributions of these two regions before the self-shielding correction is applied, resulting in a lower neutral column density than if the identical correction procedure were applied with a smaller grid spacing. This effect is not important for computing $n(z)$, the number of systems with N_{HI} above the DLA cutoff, but it can be important for computing the *total* mass density of neutral gas, Ω_{ccg} . We examined the effect by reprojecting some of the halos at $z=2,3,4$ in the SCDM model at 2 and 4 times the original spatial resolution. The original resolution of 5.43 kpc underpredicts the total HI in the simulation, while the cold collapsed gas mass in the 2X and 4X cases is nearly identical. Consequently, we regard the 2X case as numerically converged.

Unfortunately, reprojecting all the simulation outputs at this higher resolution is not computationally feasible. We therefore developed an approximate procedure based on the original grid spacing, calibrated against the few higher resolution SCDM projections. In grid cells where the self-shielding corrected HI column is greater than a threshold value $N_{\text{HI},c}$, we treat as fully neutral all gas particles that contribute to that grid cell and meet the following criteria: temperature $T < 30,000\text{K}$ and gas density $\rho_g > (1000/177)\rho_{\text{vir}}(\Omega_b/\Omega_0)$, where ρ_{vir} is the virialization overdensity described in §2.2. For critical models, the density cut corresponds to 1000 Ω_b . In subcritical models, the density cut occurs at the same fraction of the critical density as in the $\Omega_0 = 1$ models. We find that for $\log N_{\text{HI},c} = (20.4, 20.7, 20.7)$ at $z = (2, 3, 4)$ this procedure reproduces the SCDM high resolution values for Ω_{ccg} and Ω_{obs} to within 10%.

4. DLA and LL Absorption by Low Mass Halos

4.1. Motivation and method

We have so far focused on DLA and LL absorption in halos above our simulation mass resolution limits M_{res} . However, if we want to test cosmological models against the observed incidence $n(z)$, we must also consider the absorption that arises in lower mass halos, which are smaller in cross section but much more numerous. QKE find that a photoionizing background suppresses the collapse and cooling of gas in halos with circular velocities $v_c < v_{c,\text{min}} = 37 \text{ km s}^{-1}$. Thoul & Weinberg (1996) find a similar cutoff in much higher resolution, spherically symmetric calculations. We should therefore be able to compute the total incidence $n(z)$ in our

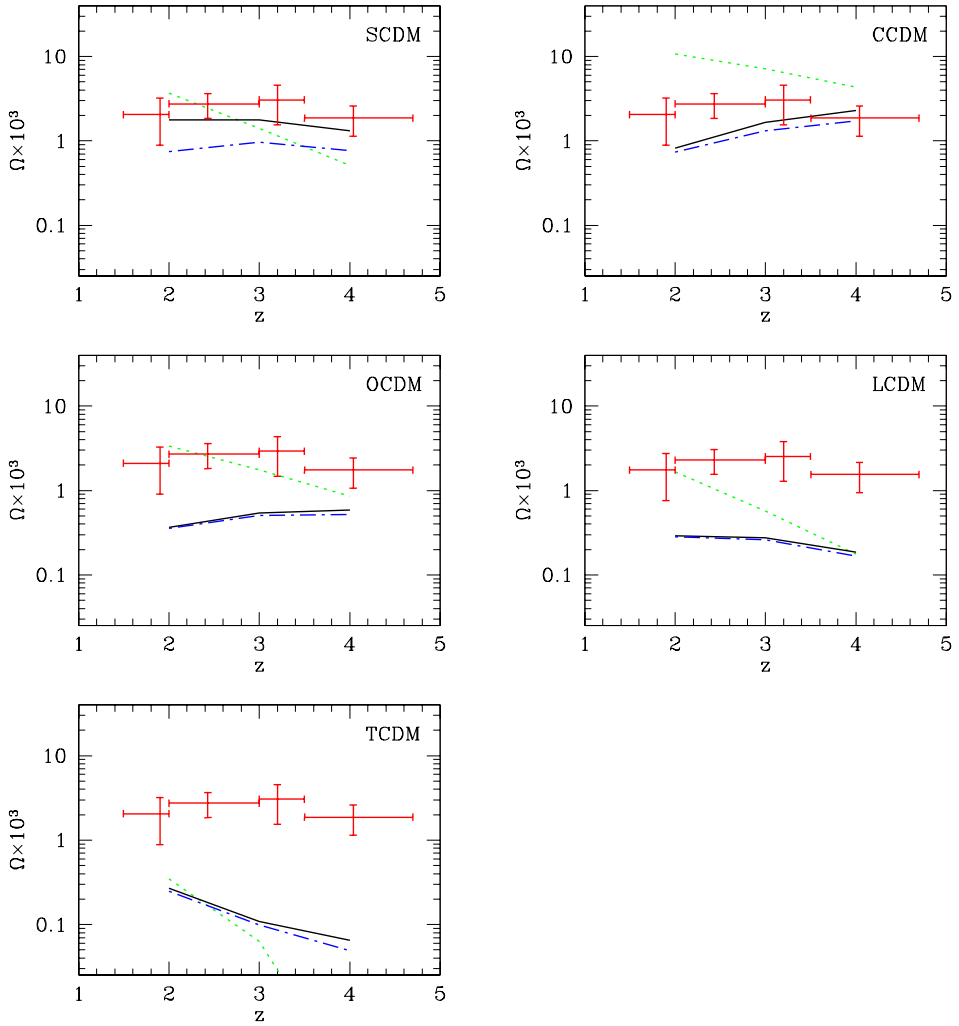


Fig. 4.— Fraction of critical density in cold collapsed gas and stars in halos $v_c \geq v_{c,res}$. The solid lines are the density parameter Ω_{ccg} in cold collapsed gas for each cosmological model. The dotted lines are Ω_* , the same quantity for the stars. The dot-dashed lines plots the “observational” values of Ω_{ccg} , which include only lines of sight with HI columns $N_{\text{HI}} < 10^{21.8} \text{ cm}^{-2}$. The 1σ error crosses are taken from Storrie-Lombardi et al. (1996b) and adjusted for the appropriate cosmology.

five cosmological models by accounting for absorption in halos with $v_{c,min} < v_c < v_{c,res}$. As discussed in §2.1, $v_{c,res}$ is approximately 125 km s^{-1} in the critical models and 80 km s^{-1} in the subcritical models at $z = 2$.

Our approach to this problem is similar to that of GKHW, though there are important differences of detail that make a significant difference to the end results, as we discuss later. We compute the number density of halos as a function of mass at specified redshift using the Press-Schechter approximation:

$$N(M, z) dM = \sqrt{\frac{2}{\pi}} \frac{\rho_0}{M} \frac{\delta_c}{\sigma_0} \left(\frac{\gamma R_f}{R_*} \right)^2 \exp \left(\frac{-\delta_c^2}{2\sigma_0^2} \right) dM, \quad (1)$$

where ρ_0 is the mean comoving mass density, R_f is the Gaussian filter radius corresponding to mass $M = (2\pi)^{3/2} \rho_0 R_f^3$, and δ_c is the critical linear density contrast that corresponds to gravitational collapse. The parameters σ_0 , γ and R_* are related to moments of the power spectrum (Bardeen et al. 1986). We use our numerical simulations to calibrate the function $\alpha(v_c, z)$, the mean cross section for DLA (or LL) absorption of halos with circular velocity v_c at redshift z . Multiplying $N(M, z)$ by $\alpha(v_c, z)$ and integrating from v_c to infinity yields the number of DLA (LL) absorbers per unit redshift residing in halos of circular velocity greater than v_c :

$$n(z, v_c) = \frac{dr}{dz} \int_{M(v_c)}^{\infty} N(M', z) \alpha(v'_c, z) dM', \quad (2)$$

where v'_c is the circular velocity at the virial radius of a halo of virial mass M' , and r is comoving distance (see GKHW for detailed discussion). Taking the lower limit of the integral to be $v_{c,min}$, the minimum circular velocity for gas cooling and condensation, yields $n(z)$, the total incidence of DLA (or LL) absorption at redshift z .

Both QKE and Thoul & Weinberg (1996) find that photoionization has little effect on the amount of gas that cools in halos with $v_c \gtrsim 60 \text{ km s}^{-1}$, consistent with the results of Navarro & Steinmetz (1997) and Weinberg et al. (1997). Therefore, it is reasonable to assume that the behavior of $\alpha(v_c, z)$ in the circular velocity range $60 \text{ km s}^{-1} \lesssim v_c \lesssim v_{c,res}$ can be extrapolated from our standard simulations. For lower mass halos, we must apply a damping function that cuts off smoothly at $v_{c,min}$, to account for the suppression of gas condensation by photoionization. To help calibrate this damping function, we employ the two higher resolution simulations of smaller mass halos in the SCDM model (with $\Omega = 1$, $h = 0.5$, $\Omega_b = 0.05$) performed by GKHW. These simulations have the same initial conditions, cosmological parameters, and numerical parameters as those of QKE, but they use the UV background spectrum described in §2.1. Each simulation models a $5h^{-1} \text{ Mpc}$ (comoving) periodic volume, which is evolved using a hierarchical grid of particles in the initial conditions. The central region forms a collapsed object represented by a large number of low mass particles, while regions further away are represented by a smaller number of more massive particles. A simulation of the full volume at uniform resolution equal to that of the central region would require 256^3 particles of each species. The nesting technique allows us to

achieve high resolution locally while preserving the cosmological context of the calculation. The mean circular velocity of the halos that form in these simulations is $v_c \approx 50 \text{ km s}^{-1}$.

We model $\alpha(v_c, z)$ as the product of a power law and a cutoff function,

$$\alpha(v_c, z) = \alpha_{\text{PL}}(v_c, z) \times \alpha_{\text{cut}}(v_c, z), \quad (3)$$

with

$$\alpha_{\text{PL}}(v_c, z) = A v_c^B \quad (4)$$

and $\alpha_{\text{cut}}(v_c, z)$ given by equation (5) below. We determine the parameters of $\alpha_{\text{PL}}(v_c, z)$ separately at $z = 2, 3$, and 4 in each cosmological model for DLA and LL absorption. For brevity, we describe our fitting procedure in the context of DLA systems; the procedure for LL systems is identical, except that cutoff in column density is $N_{\text{HI}} \geq 10^{17.2} \text{ cm}^{-2}$ rather than $N_{\text{HI}} \geq 10^{20.3} \text{ cm}^{-2}$.

Halos are binned in 0.05 dex increments in $\log v_c$, beginning with $v_{c,\text{res}}$ and subject to the constraint that there be at least 10 halos in each bin. We sometimes are forced to widen the bin size to satisfy the latter constraint. Let σ_{DLA} denote the “cross section” of DLA absorption, i.e. the comoving area subtended by HI column densities $N_{\text{HI}} \geq 10^{20.3} \text{ cm}^{-2}$ when a halo is projected onto a plane. For the binned distribution of halos, we determine the log of the average halo DLA absorption cross section, $\log\langle\sigma_{\text{DLA}}\rangle$ for each bin. Then we calculate the statistical uncertainty of $\log\langle\sigma_{\text{DLA}}\rangle$ in each bin by using the bootstrap method with 1000 random realizations of the data set of halos with $M \geq M_{\text{res}}$. The distribution of halo cross sections σ_{DLA} at a given v_c is approximately log-normal and hence best described by a Gaussian in log space. Since we will use the bootstrap errors in the next section to calculate confidence limits, which assume Gaussianity, we express the errors in log space. We fit the points $\log\langle\sigma_{\text{DLA}}\rangle$ by linear least squares to determine the parameters A and B of equation (4), the amplitude and index of $\alpha_{\text{PL}}(v_c, z)$. The error crosses in Figures 5-7 show the mean absorption cross section in each bin of circular velocity at redshifts $z = (2, 3, 4)$ for DLA and LL systems in the SCDM model and at $z = 3$ for the other models. The horizontal error bars show the width of each bin, and the vertical error bars show the 1σ logarithmic uncertainty in $\langle\sigma_{\text{DLA}}\rangle$ for the bin determined by the bootstrap procedure. Error crosses at $v_c = 50 \text{ km s}^{-1}$ show $\langle\sigma_{\text{DLA}}\rangle$ and the 1σ logarithmic uncertainty for halos in the high resolution SCDM simulations.

Figures 5-7 also show the absorption cross section for each individual resolved halo in the simulations. The number of vertices on each point indicates the number of SKID-identified concentrations of cold collapsed gas within the halo. There are two competing effects that determine the trend between absorption cross section and circular velocity. Higher mass halos have deeper potential wells, causing the concentrations of cold gas to contract further, explaining the downward trend in cross section with circular velocity exhibited by points with a fixed number of vertices. However, more massive halos tend to harbor more than one concentration of gas, increasing their absorption cross section. The overall trend is that halos of higher circular velocities on average have larger absorption cross sections. This complex gas dynamical behavior

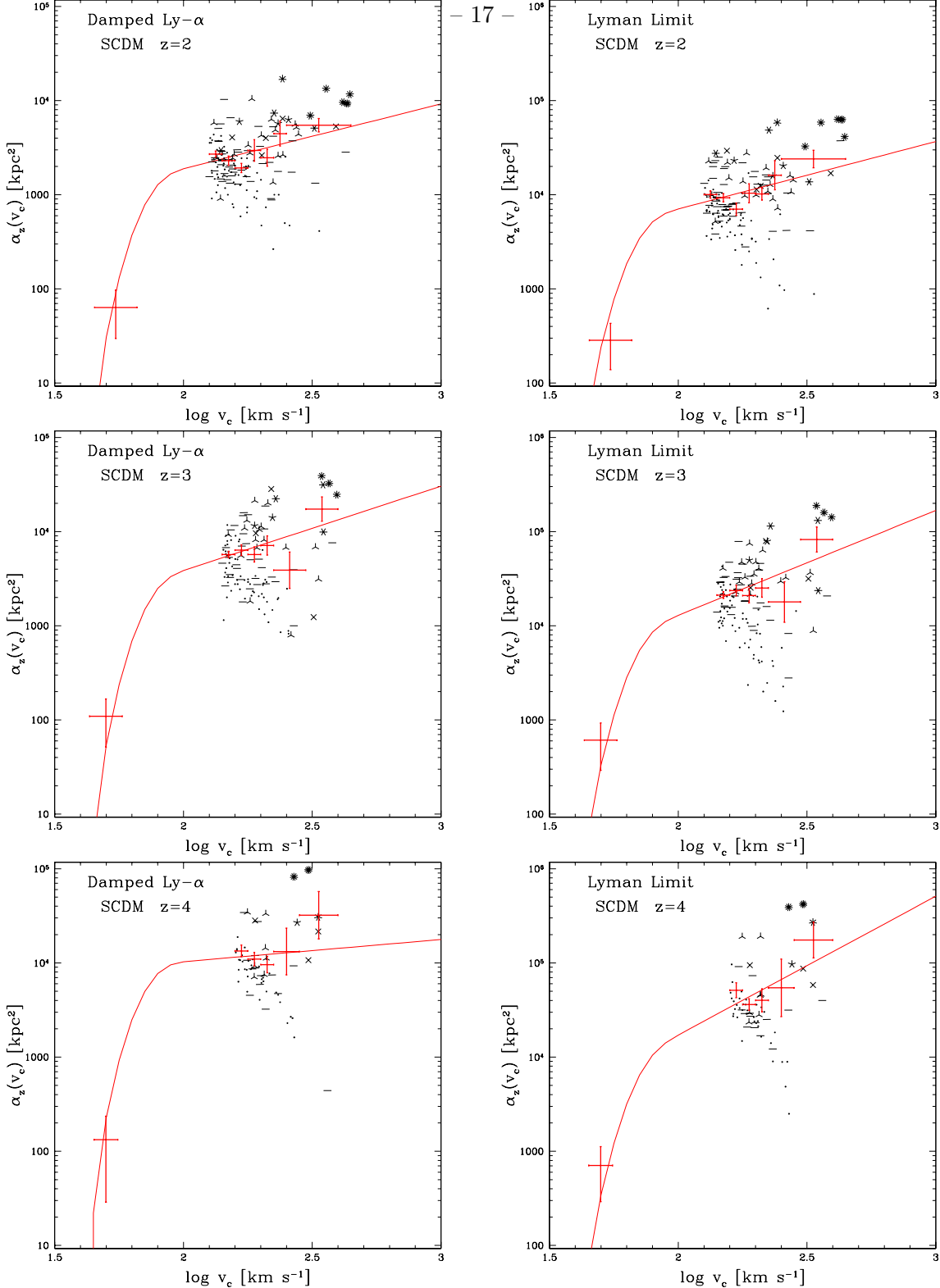


Fig. 5.— Comoving absorbing area in kpc^2 vs. circular velocity v_c in km s^{-1} for simulated halos. Left hand panels show the area for DLA absorption, $N_{\text{HI}} \geq 10^{20.3} \text{ cm}^{-2}$, and right hand panels for Lyman limit absorption, $N_{\text{HI}} \geq 10^{17.2} \text{ cm}^{-2}$. The points lying at $v_c \geq 100$ denote halos in the 22.22 Mpc simulation, where the number of vertices in each data point corresponds to the number of gas concentrations in the halo, with the solid points representing halos containing a single absorber. The solid line shows the fitted smooth relation $\alpha(v_c, z)$

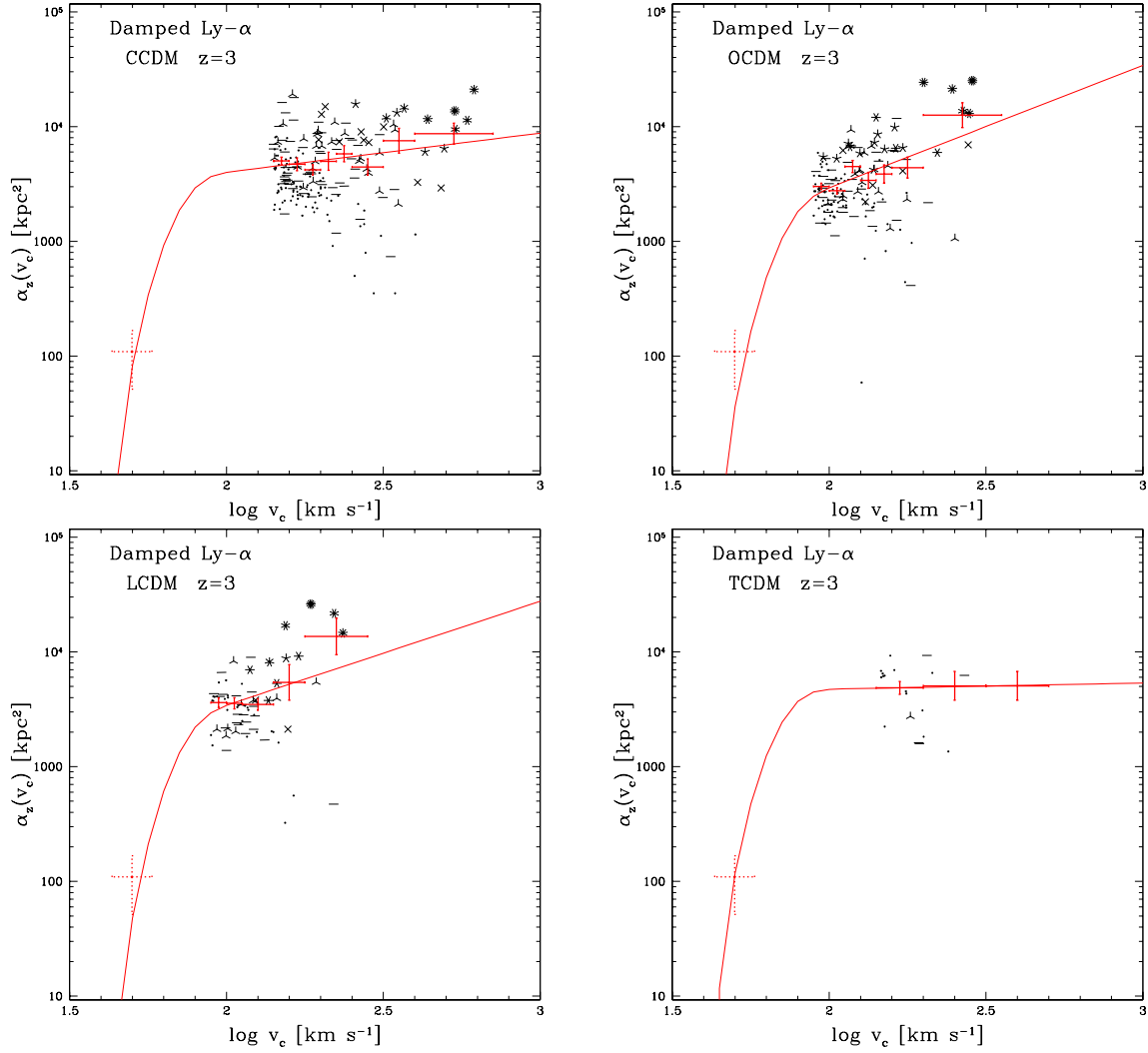


Fig. 6.— As in Figure 5 except for DLA systems in the other four models at $z = 3$. The dotted cross hairs denote the data from the high resolution SCDM simulations.

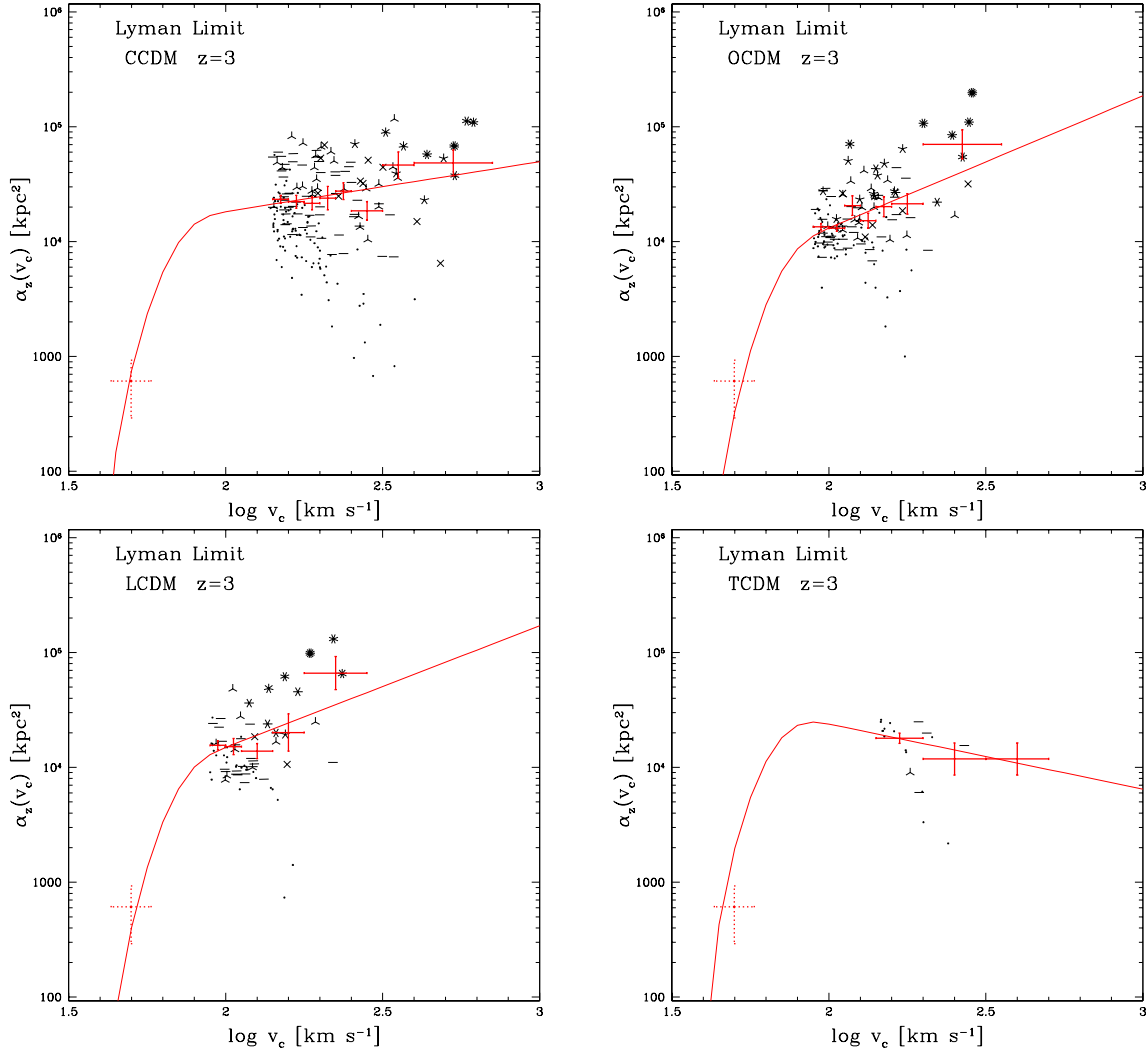


Fig. 7.— As in Figure 5 except for Lyman limit systems in the other four models at $z = 3$. The dotted cross hairs denote the data from the high resolution SCDM simulations.

demonstrates the value of a fully numerical treatment of the absorption cross section over a semi-analytic approach.

It is important to note that we are not seeking to model the *distribution* of absorption cross sections in each bin, but only to characterize the *mean* cross section in each bin so that the total absorption can be accurately reconstructed from equation (2). The large spread and asymmetry in the distribution of absorption cross sections for individual halos is inconsequential for our purposes: $\alpha(v_c, z)$ is the number which, when multiplied by the halo number density at v_c , yields the total absorption at that v_c that matches the total absorption present in the simulation. The bootstrap technique yields a robust estimate of the statistical uncertainty in this mean cross section caused by the finite number of halos in the simulation. Although the spread in absorption cross sections of individual halos may be large, their average absorption is a well determined quantity.

For the damping function, we assume an exponential cutoff that depends on halo virial mass (proportional to v_c^3):

$$\alpha_{\text{cut}}(v_c, z) = 1 - \exp(-(v_c - v_{c,\text{min}})^3 / \Delta^3), \quad (5)$$

where $v_{c,\text{min}}$ is the minimum circular velocity for DLA and LL absorption and Δ is the width in km s^{-1} of the exponential. In GKHW we used a cutoff that was exponential in $(v_c - v_{c,\text{min}})$ rather than $(v_c - v_{c,\text{min}})^3$, but with the new form our fits for $\alpha(v_c, z)$ agree better with the results of our simulations of subcritical models (which extend to lower v_c than the SCDM simulation available to GKHW) and with preliminary results from a higher resolution simulation of the LCDM model. We choose the value of Δ so that the product $\alpha_{\text{PL}}(v_c, z)\alpha_{\text{cut}}(v_c, z)$ for the SCDM model passes through the data points from the high resolution simulations described above. We find that the value $\Delta = 34 \text{ km s}^{-1}$ works well for all three redshifts, $z = 2, 3, 4$. We choose $v_{c,\text{min}}$ to be 40 km s^{-1} for DLA systems and 37 km s^{-1} for LL systems, since, having chosen Δ to be the same for DLA and LL systems, these slightly differing values of $v_{c,\text{min}}$ provide the best fit through the high-resolution points. Since we have no high resolution simulations for other cosmological models, we assume the same cutoff parameters for all the models. Consequently, $\alpha(v_c, z)$ in equation (3) is the product of a power law $\alpha_{\text{PL}}(v_c, z)$ that is fit separately for each redshift and cosmological model and a cutoff $\alpha_{\text{cut}}(v_c, z)$ that is the same for each redshift and each cosmological model. Although this approach is to some extent dictated by our available simulations, it is physically plausible if the cutoff at low v_c is indeed driven mainly by the physics of photoionization and gas cooling, which is cosmology independent.

Smooth curves in Figures 5-7 show the fitted $\alpha(v_c, z)$ relations, and these are shown together for all models and redshifts in Figure 8. The values of the fit parameters and their 1σ uncertainties are listed in Table 2.

Figure 8 also shows the $\alpha(v_c, z)$ relations that we derived for the SCDM model in GKHW, which are substantially different from those derived here. The differences result from our use of bootstrap error estimates in place of simple $1/\sqrt{N}$ Poisson error bars, from our adoption of a more conservative resolution cutoff $v_{c,\text{res}}$, and from the change in shape of the assumed damping

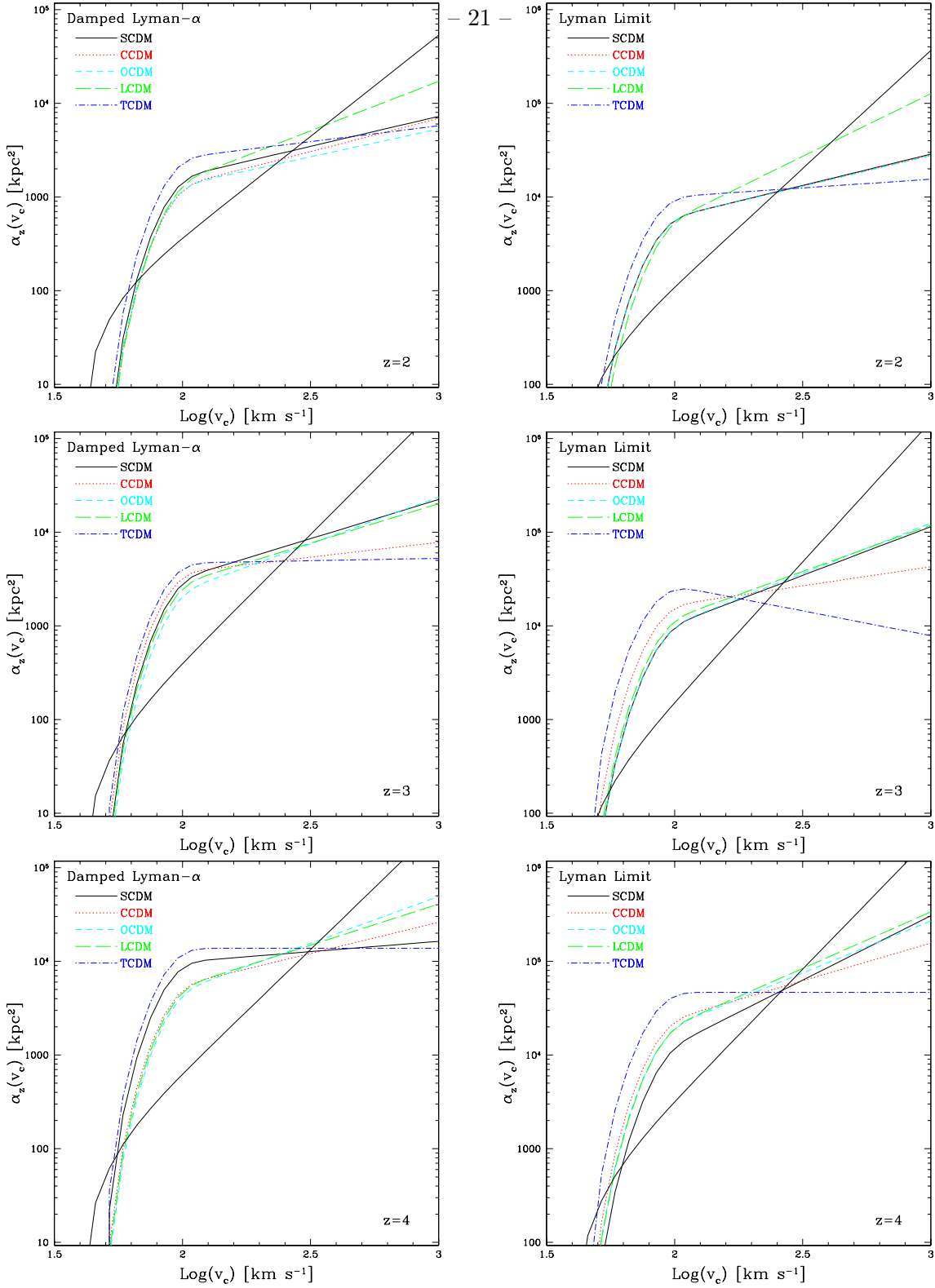


Fig. 8.— The absorption cross sections $\alpha(v_c, z)$ plotted from each model for DLA and Lyman limit systems. The area is given in comoving kpc^2 . The more highly inclined solid curves are the fits for the SCDM model from GKHW. In the upper and middle right panel, OCDM falls nearly on top of the SCDM curve. In the upper right, the CCDM curve is also similar to SCDM.

cutoff discussed above. In GKHW, the large $1/\sqrt{N}$ error bars and the depression of absorption in the lowest v_c bin because of resolution effects allowed us to fit a single, fairly steep power law between the $v_c \approx 50 \text{ km s}^{-1}$ points from the high resolution simulations and the points at $v_c \geq 100 \text{ km s}^{-1}$ from the standard simulation. The damping function $\alpha_{\text{cut}}(v_c, z)$ did not substantially affect absorption until $v_c \lesssim 50 \text{ km s}^{-1}$. With the smaller, and more believable, bootstrap errors and the more conservative $v_{c,\text{res}}$ value, we fit shallower power laws to the high v_c points, and the new damping function cuts off these power laws so that the $\alpha(v_c, z)$ curves go through the $v_c = 50 \text{ km s}^{-1}$ points. These new fits agree better with the results of the subcritical models (not available to GKHW), for which the numerical results extend to $v_{c,\text{res}} \approx 80 \text{ km s}^{-1}$ and clearly rule out a single power law fit reaching down to $v_c = 50 \text{ km s}^{-1}$. They also agree better with preliminary results from a higher resolution simulation of the LCDM model. The net impact of the new fitting procedure is to increase $\alpha(v_c, z)$ in the range $55 < v_c < 220 \text{ km s}^{-1}$. Because many high-redshift halos lie in this v_c range, the overall effect will be to increase our predictions for the total incidence $n(z)$ in all cosmological models, relative to the predictions in GKHW and GKWH.

Because of the small number of resolved halos in the TCDM model at $z = 3$, and 4, we were unable to obtain fits that we consider reliable. Indeed, to obtain fits for TCDM at these redshifts in the first place, we artificially added a point at high v_c with the same value and error bar as the point next to it based on the simulation (see the TCDM panels of Figures 6 and 7). At $z = 4$, there is only one v_c bin with resolved halos, so this replication forces the slope of $\alpha_{PL}(v_c, z)$ to zero. At $z = 3$, the slope for DLA systems is close to zero and the slope for LL systems is actually negative — more absorption in lower v_c halos. The result of these fits is to give a large cross-sectional area to halos with $v_{c,\text{min}} < v_c < v_{c,\text{res}}$. We therefore regard our results for $n(z)$ in the TCDM model at $z = 3$ and 4, given below, as extreme upper limits to the true incidence of DLA and LL absorption in this model.

4.2. Estimating the Contribution of Low Mass Halos

We are now in a position to correct the $n(z)$ estimates from §3 to include the contribution from halos with $M < M_{\text{res}}$. We employ two different procedures for calculating the correction, both of them based on the $\alpha(v_c, z)$ results from §4.1. In Method A, we assert that the halo mass function of the simulation is correct above M_{res} , and we therefore adjust δ_c in the Press-Schechter relation so that the total number of Press-Schechter halos above M_{res} matches that in the simulation. Hence, we use Press-Schechter only to compute the absorption by halos with $M < M_{\text{res}}$, which we add to the numerical results for $M \geq M_{\text{res}}$. In Method B, we assume that the Press-Schechter mass function with $\delta_c = 1.69$ is correct for each cosmological model and do not attempt to match it to the simulated mass function, allowing for the possibility that the finite volume of our simulations affects the number of halos. In this method, we use the simulation data only to determine the relation $\alpha(v_c, z)$ and otherwise rely exclusively on Press-Schechter. Figure 9 plots the cumulative number density of halos in each model in the simulation and in Press-Schechter with $\delta_c = 1.69$. In

cases other than TCDM, the number density of halos in the simulation tends to be less than the number density predicted by $\delta_c = 1.69$ Press-Schechter. Consequently, estimates of the absorption by Method A tend to be lower than those of Method B.

For Method A, we adjust the value of δ_c at each simulation output so that the cumulative number density of halos $N_{PS}(> v_{c,res})$ matches the simulated value $N_{sim}(> v_{c,res})$. We calculate the low mass halo contribution by integrating (2) from $v_{c,min}$ to $v_{c,res}$ and add this to the absorption present in the simulation, i.e. the sum of all halos with $v_c > v_{c,res}$. Method B integrates (2) throughout the entire mass range that DLA and Lyman limit absorption occurs, $v_{c,min} < v_c < \infty$, using $\delta_c = 1.69$. Unlike Method A, Method B uses $\alpha(v_c, z)$ over the entire mass range, not just in the regions where the simulation does not resolve halos.

Figures 10 and 11 show the cumulative incidence for each model and each method. Errors in $n(z)$ resulting from (2) are determined by first calculating the 68.3% confidence ellipse of the χ^2 fit of the power law to the binned halos in Figures 5-7. $n(z)$ is calculated for each pair of slope-intercept values along the error ellipse, thereby yielding a range of values taken to be the 68.3% confidence range in $n(z)$. For Method B, this is the total error. For Method A, this error is added in quadrature to the error of the simulated data, which we calculate by bootstrap resampling the halo distribution. Table 3 gives the incidence calculated using both methods as well as the ratio of $n(z, v_{c,res})$, the incidence due only to halos resolved in the simulation, to the total incidence $n(z)$.

The absorption cross section of massive ($v_c \approx 200 \text{ km s}^{-1}$) halos is quite small compared to smaller mass halos, independent of the method used. In SCDM, for example, less than 10% of the total DLA cross section is contributed by halos with $v_c > 160 \text{ km s}^{-1}$ at any of the three redshifts. In the subcritical models, halos larger than $v_c > 160 \text{ km s}^{-1}$ typically account for only 10%-15% of the total absorption cross-section. The Lyman limit systems behave similarly. Consequently, our models predict that most DLA and LL absorption arises in smaller mass halos.

4.3. Other Possible Sources of Absorption

It is possible that some Lyman limit and/or DLA absorption originates from regions other than galactic halos. To investigate this alternative within our simulations, we project the entire simulation volume and compare the area of LL and DLA absorption to the sum of the absorption calculated by projecting each halo individually. In the analysis presented here, we use all halos that have at least one group identified by SKID as described in section 2.2 (i.e. at least one concentration of cold gas that is gravitationally bound), whether or not the halo itself has $M \geq M_{res}$. Above $M = M_{res}$, 98% of the dark matter halos harbor at least one SKID-identified group.

For all models except TCDM (which has few halos above our resolution limit), we calculate the total area subtended by DLA absorption in the halos with SKID-identified groups. Comparing

Damped Ly α						
Model	z = 2		z = 3		z = 4	
	A	B	A	B	A	B
SCDM	0.436	0.686	0.329	0.895	2.075	0.235
CCDM	0.204	0.760	1.454	0.340	0.919	0.712
OCDM	0.438	0.638	-0.133	1.066	0.177	1.069
LCDM	-0.461	1.132	0.259	0.904	0.464	0.940
TCDM	1.262	0.361	2.100	0.0532	2.670	0.000

Lyman Limit						
Model	z = 2		z = 3		z = 4	
	A	B	A	B	A	B
SCDM	0.952	0.715	0.416	1.113	-0.182	1.474
CCDM	0.970	0.704	1.924	0.434	1.269	0.862
OCDM	0.988	0.696	0.349	1.151	0.568	1.191
LCDM	-0.453	1.434	0.592	1.057	0.378	1.291
TCDM	2.155	0.199	4.042	-0.567	3.201	0.000

Table 2: Fitted parameter values for $\alpha_{\text{PL}}(v_c, z) \equiv Av_c^B$.

Damped Ly α									
Model	z = 2			z = 3			z = 4		
	$n_A(z)$	$n_B(z)$	$f(v_{c,res})$	$n_A(z)$	$n_B(z)$	$f(v_{c,res})$	$n_A(z)$	$n_B(z)$	$f(v_{c,res})$
SCDM	0.281	0.335	0.171	0.493	0.565	0.114	1.152	1.295	0.036
CCDM	0.258	0.263	0.174	0.654	0.697	0.107	1.003	1.221	0.104
OCDM	0.131	0.169	0.618	0.216	0.266	0.500	0.346	0.548	0.322
LCDM	0.111	0.163	0.649	0.135	0.206	0.422	0.175	0.280	0.263
TCDM	0.191	0.260	0.084	0.219	0.231	0.027	0.446	0.296	0.013

Lyman Limit									
Model	z = 2			z = 3			z = 4		
	$n_A(z)$	$n_B(z)$	$f(v_{c,res})$	$n_A(z)$	$n_B(z)$	$f(v_{c,res})$	$n_A(z)$	$n_B(z)$	$f(v_{c,res})$
SCDM	1.191	1.391	0.161	1.819	2.071	0.123	1.867	2.206	0.093
CCDM	1.306	1.285	0.152	3.352	3.526	0.103	4.953	6.009	0.105
OCDM	0.670	0.870	0.551	1.108	1.314	0.479	1.741	2.664	0.341
LCDM	0.487	0.727	0.618	0.648	0.996	0.377	0.797	1.264	0.266
TCDM	0.869	1.155	0.066	1.612	1.697	0.013	1.861	1.252	0.010

Table 3: DLA and LL incidence determined by correction methods. The first two columns for each redshift denote the total incidence $n(z)$ found using methods A and B. The third column $f(v_{c,res})$ is the ratio of the incidence in halos resolved by the simulation to the total incidence found by Method A, that is $f(v_{c,res}) = n(z, v_{c,res})/n_A(z)$.

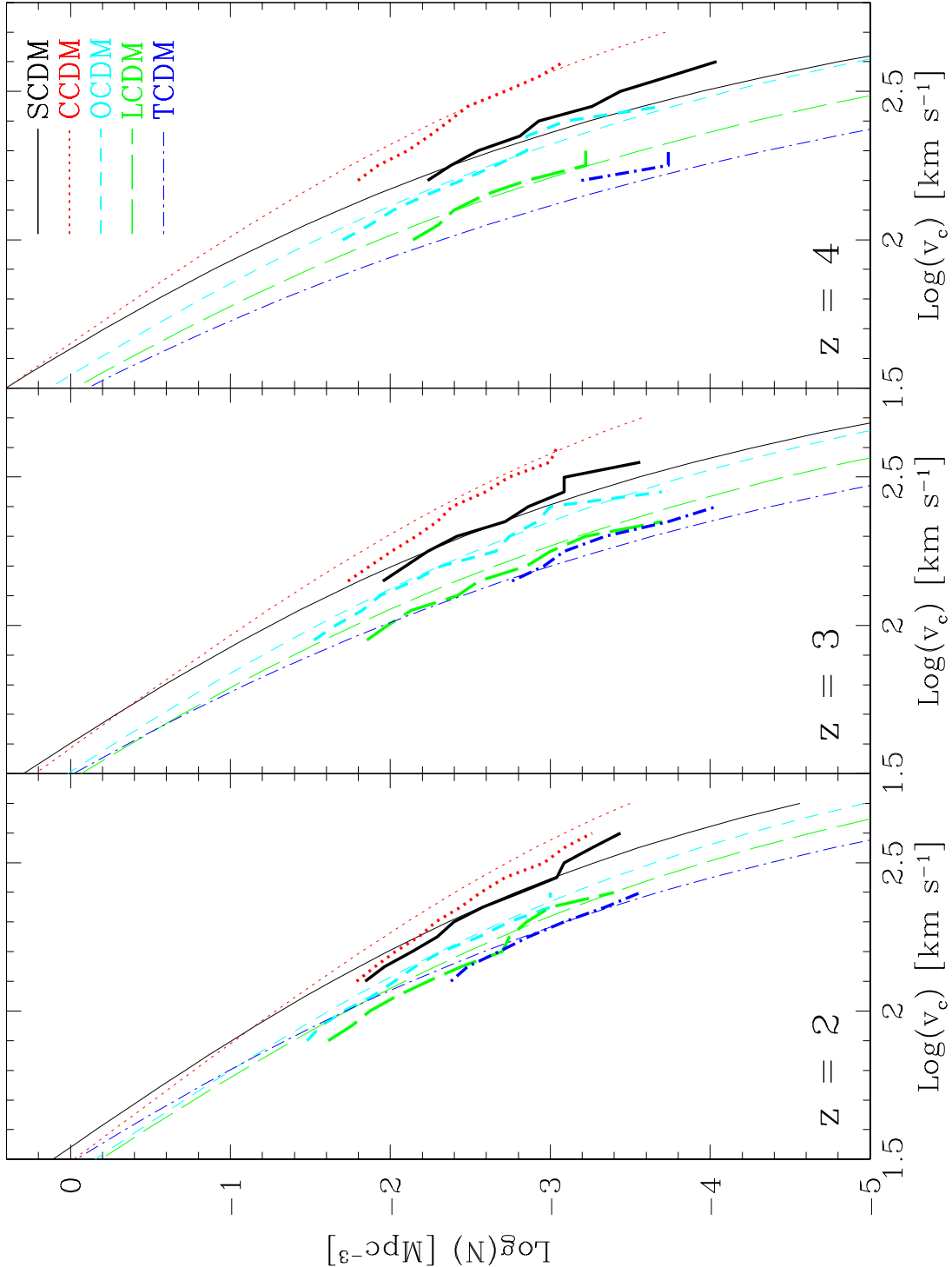


Fig. 9.— Cumulative comoving number density of halos in each model according to the simulation (thick lines) and Press-Schechter with $\delta_c = 1.69$ (thin lines).

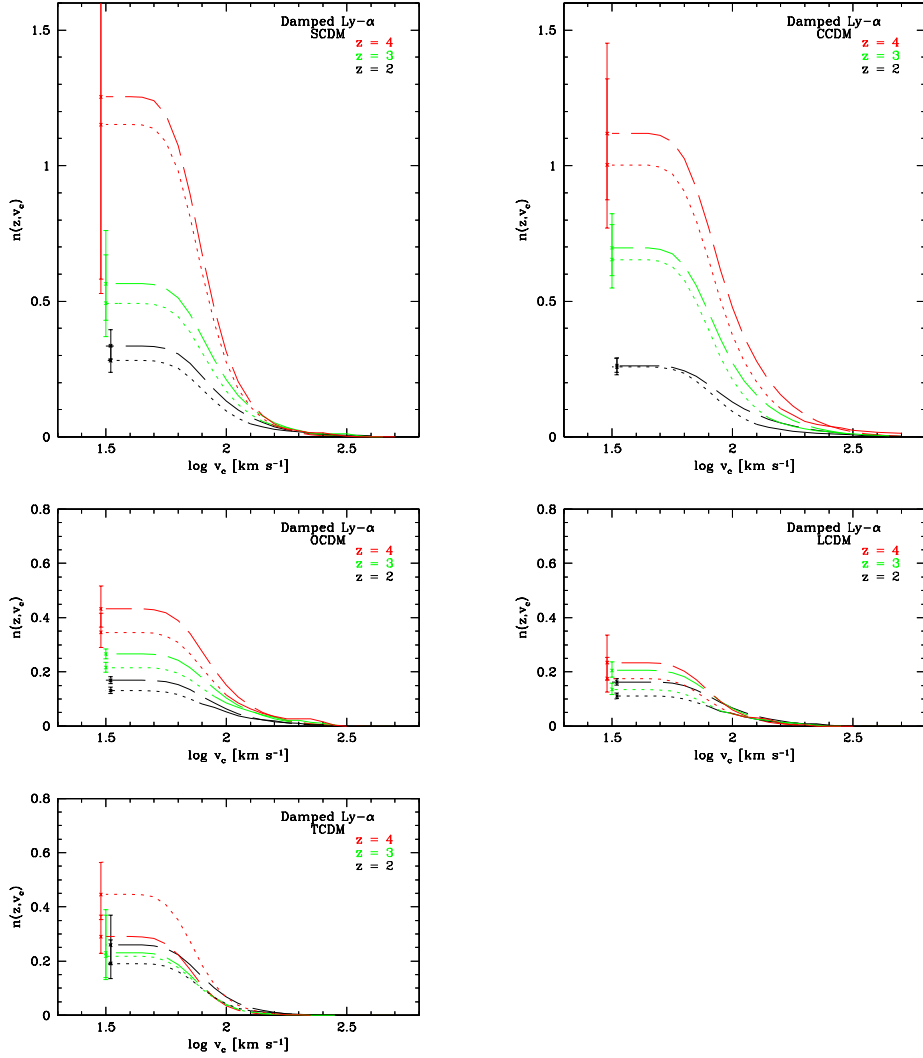


Fig. 10.— Cumulative incidence $n(z, v_c)$ of DLA systems for each model at $z = 4, 3, 2$ (from top to bottom in each panel). $n(z, v_c)$ is the number of DLA systems per unit redshift that are associated with halos of a circular velocity of at least v_c . The dotted/solid curves show the results of Method A, with the dotted portion denoting the range over which Press-Schechter is used, and the solid portion towards higher v_c denoting the range calculated directly from the simulation. The long-dashed curves show the results of Method B. Indicated on the left are the final errors of each measurement of $n(z)$, which have been plotted slightly offset from one another for greater clarity. In general, the lines denoting each method follow a progression from $z = 4$ at the top to $z = 2$ at the bottom. The only exception is the $z = 2$ dashed line in TCDM which is slightly above the $z = 3$ dashed line.

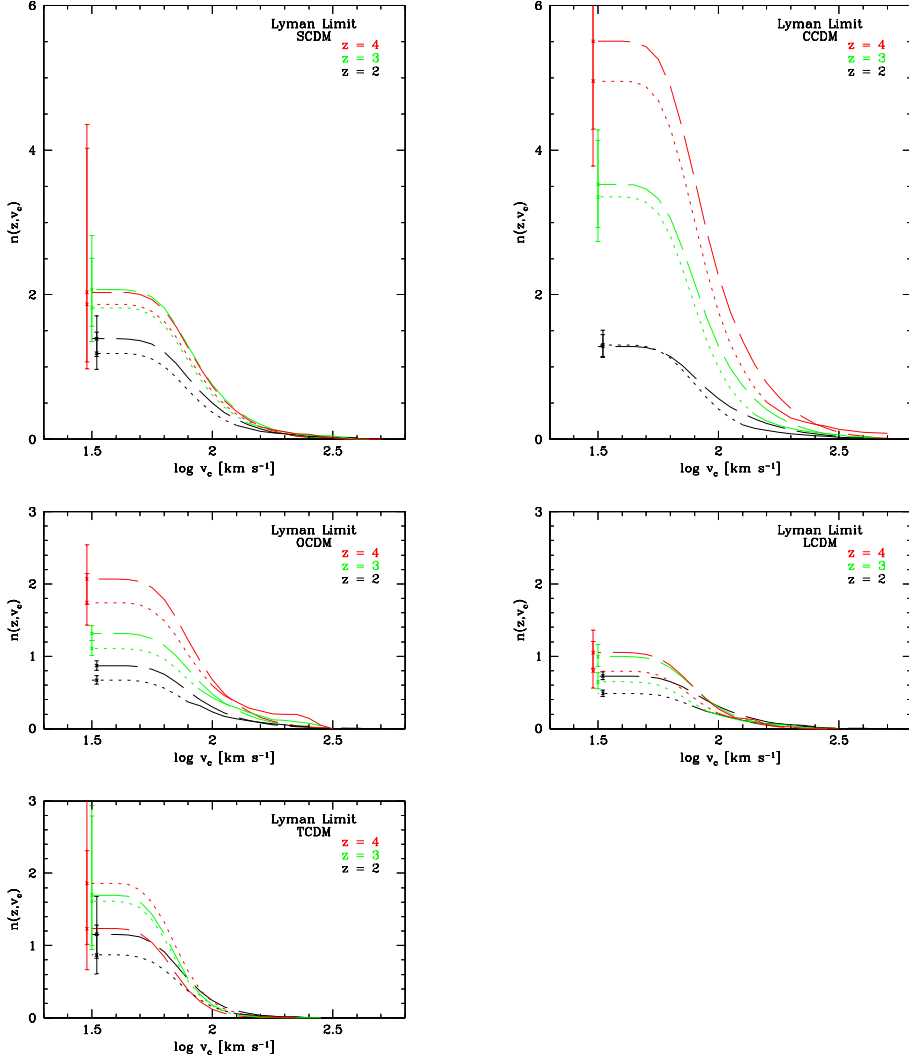


Fig. 11.— As in Figure 10 but for Lyman limit systems. The lines denoting each method generally follow a progression from $z = 4$ at the top to $z = 2$ at the bottom. The only exceptions are SCDM where the $z = 3$ dashed line is slightly above the $z = 4$ dashed line at low v_c and TCDM where the dashed lines follow the top-to-bottom progression $z = 3, 4, 2$ at low v_c .

this value to the total area subtended in an entire volume projection of each simulation at redshifts $z = 2$ and $z = 4$, we find agreement within 4.5% for all the models at both redshifts, and to better than 2% in five of the eight cases. We attribute the remaining differences to having more than one absorber along a given line of sight. Hence, all DLA absorption in the simulation occurs within halos with at least one concentration of cold, gravitationally bound gas.

In LL absorption, five of the eight outputs agree to better than 6% when compared in this manner. However, at $z = 4$ the results of volume projection and halo projection differed by 15%, 30%, and 13% for SCDM, CCDM, and OCDM respectively. We took the worst case, $z = 4$ CCDM, and projected all the halos that contained at least 32 particles (gas + dark matter), whether or not they contained a SKID-identified gas concentration. When we sum the area subtended by LL absorption in these halos, we find that it now accounts for all but 1.2% of the LL absorption found by projecting the entire volume. Hence Lyman limit absorption still occurs exclusively in halos, but in this instance 30% of it occurs in halos in which our resolution of gas dynamics and cooling is only marginal and in which there are no SKID-identified gas concentrations. If our study had higher resolution, it is likely that some of these halos would have been able to form DLA systems as well. However, it is just to correct for these unresolved or under-resolved halos that we developed our Press-Schechter correction technique. The important conclusion is that all the Lyman limit absorption we observe can be accounted for in dark matter halos. If Lyman limit absorption were to occur outside galactic halos, it would have to be in regions that are much too small for us to resolve.

To summarize, all DLA and LL absorption in our simulations occurs in dynamically bound dark matter halos, even below our resolution cutoff. At $z = 2$ and $z = 4$, in all four of the models tested, DLA absorption arises entirely in objects identified by SKID as bound concentrations of cold gas. LL absorption in the simulations also occurs exclusively in dark matter halos, although at $z = 4$ some of the gas within these halos is able to reach LL column densities without becoming a SKID-identified concentration.

5. Implications for Absorption in Cosmological Models

Figures 12 and 13 are similar to Figures 1 and 2 but show values of $n(z)$ that have been corrected for the unresolved halos. We plot the average of the results of our two correlation procedures A and B (§4.2, Table 3), with error bars that are the average of the error bars from these two procedures. With the contributions of low mass halos included, all the models are consistent with the observed numbers of DLA absorbers, while all except LCDM are consistent with the observed numbers of LL absorbers at the 2σ level. Note, however, that we consider our values for the TCDM model at $z = 3$ and 4 to be upper limits, for the reasons discussed in §4.1 and recapped briefly below.

SCDM was the model treated by GKHW (with a slightly different background radiation

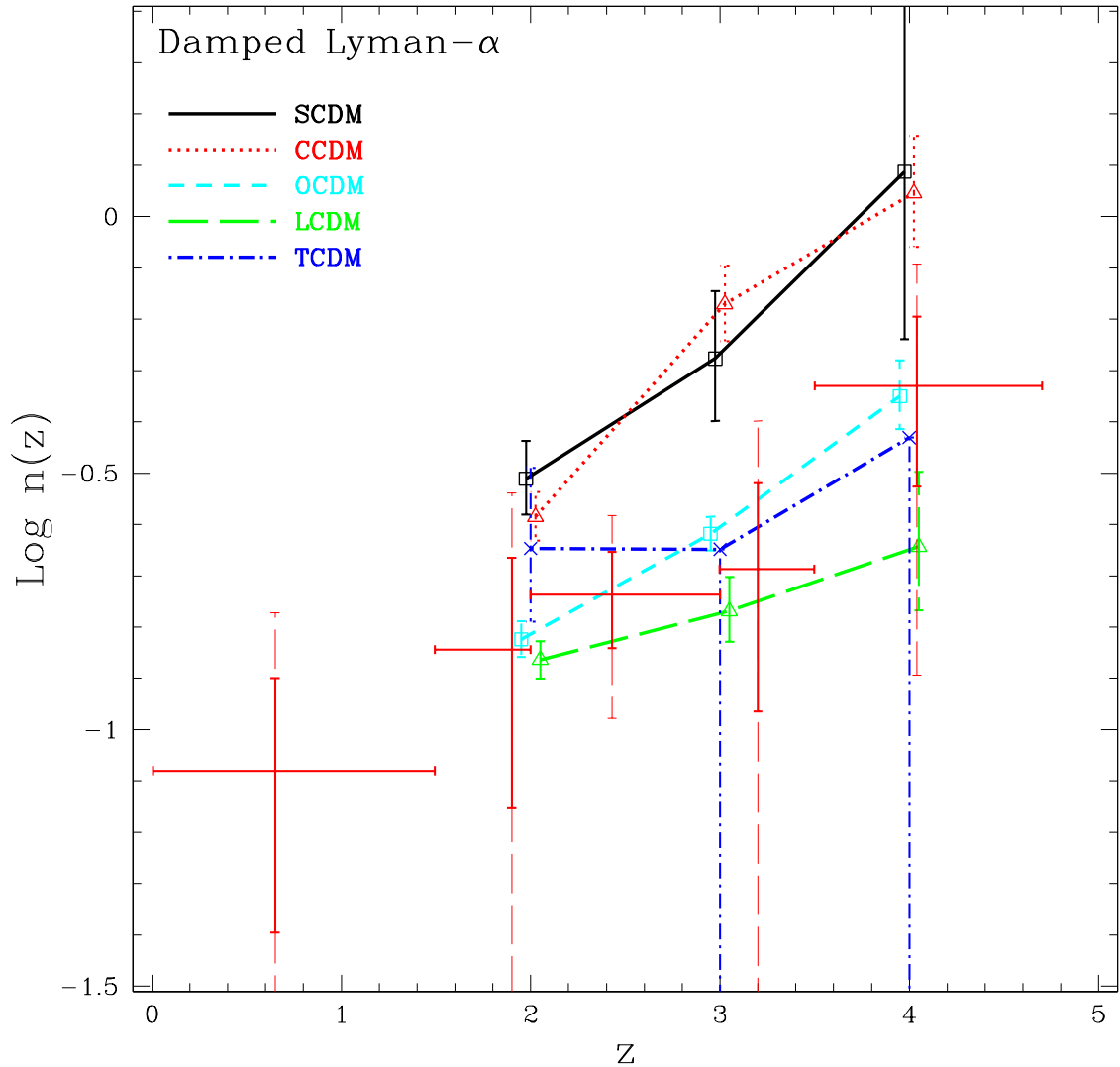


Fig. 12.— The predicted number $n(z)$ of DLA systems per unit redshift for various cosmological models vs. observational data. Notation is as in Figure 1. We evaluate all models at the same redshifts $z = 2, 3, 4$ but plot them with slightly offset z values for greater clarity.

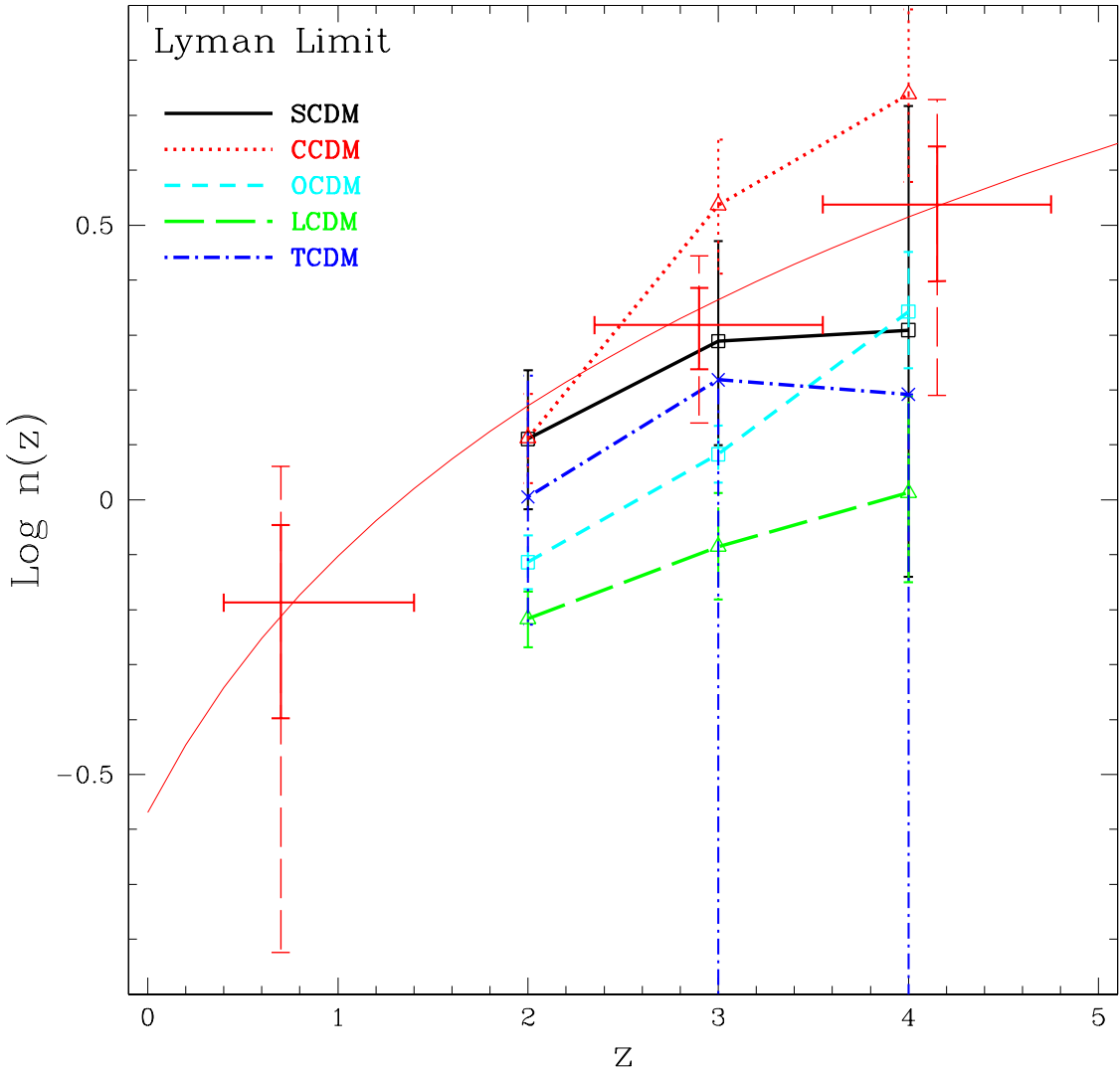


Fig. 13.— The predicted number $n(z)$ of Lyman limit systems per unit redshift for various cosmological models vs. observational data. Notation is as in Figure 2. As in Figure 12, we evaluate all models at the same redshifts $z = 2, 3, 4$ but plot them with slightly offset z values for greater clarity.

field). GKHW found that SCDM matched the DLA observations and fell below the LL observations, but with our improved treatment SCDM now exceeds the observed DLA values and the underproduction of LL absorption has been eliminated.

CCDM and SCDM now produce similar amounts of DLA absorption, even though the mass of stars in the CCDM model is substantially higher (Figure 4). Figure 9 shows that the abundance of high mass halos ($v_c \gtrsim 150 \text{ km s}^{-1}$) is substantially higher in CCDM, as expected given its higher normalization, but the DLA cross section is dominated by less massive halos, which have similar abundances in the two models. At $z = 4$, the higher halo abundance in CCDM is compensated by the higher $\alpha(v_c)$ in SCDM (Figure 8). The CCDM model does have higher $n(z)$ for LL absorption at $z = 3$ and 4, mainly because it has higher $\alpha(v_c, z)$ in the region $v_c \sim 100 \text{ km s}^{-1}$ where most of the absorption arises. The fact that CCDM has higher $\alpha(v_c, z)$ for LL absorption but similar $\alpha(v_c, z)$ for DLA absorption may indicate that more gas is falling into the CCDM halos but that it eventually settles into denser concentrations in these more massive halos and thereby reduces the DLA cross section. However, the conclusion that CCDM produces more LL absorption than SCDM rests heavily on our extrapolation of $\alpha(v_c, z)$ to low circular velocities, so it should be treated with caution.

TCDM is a difficult model to diagnose with our simulations because at $z \geq 3$ it has very few halos above our resolution limit. As noted in §4.1, we had to artificially add points at high mass in order to fit $\alpha(v_c, z)$ at $z = 3$ and $z = 4$. The resulting fit gives halos with $v_c < 125 \text{ km s}^{-1}$ absorption cross sections that are almost certainly too large, and we therefore regard our $n(z)$ prediction for TCDM at these redshifts as upper limits. At $z = 2$, however, the number of halos is enough for a reasonable fit, and $\alpha(v_c, z)$ is higher in TCDM than in any other model. We think that this high $\alpha(v_c, z)$ reflects the relatively late structure formation in the TCDM model. Gas has fallen into the halos by $z = 2$, but it has not yet collapsed to a very high density, so it still has a relatively large cross section for DLA and LL absorption. This behavior illustrates a common theme in our results: the longer the gas within a halo has been allowed to cool quiescently, the smaller its cross section in absorption becomes. Eventually the gas will shrink to a size determined by centrifugal support, but in our simulations it appears that the size of a DLA absorber is often still boosted by non-equilibrium dynamics, much like the velocity width (Haehnelt et al. 1998). At $z = 2$, TCDM can compensate for its low halo abundance with a high $\alpha(v_c)$ and thereby match the observed incidence of DLA and LL absorption. However, the halo abundance drops rapidly at higher redshift in this model, and we suspect that higher resolution simulations would yield predictions substantially below our upper limits, and hence even further below observations.

From Figure 9 we see that OCDM and LCDM consistently produce fewer halos than the scale-invariant critical density models SCDM and CCDM. Although their σ_8 values are close to that of SCDM (Table 1) and the growth factor reduction from $z = 0$ to $z = 2 - 4$ is smaller in subcritical models, OCDM and LCDM also have redder power spectra and thus less power on these relatively small scales. The difference in power spectrum shape is especially evident at the low mass end of the mass functions in Figure 9. The cross sections $\alpha(v_c, z)$ for DLA absorption

also tend to be slightly lower in the subcritical models, so they predict substantially less DLA absorption, but their predictions agree fairly well with observed values. The LL absorption cross sections tend to be slightly higher, but not enough to compensate for the lower halo abundance. The LCDM model has fewer halos than OCDM because of the larger growth factor reduction in a flat universe, and it is at best marginally consistent with the observed LL abundance.

6. Conclusions

We can divide our conclusions into two classes, those that rely only on the results of our simulations, and those that rely on our extrapolation of these results via the Press-Schechter method to account for absorption by low mass halos. We will treat these two classes of conclusions in turn.

Our simulations resolve the formation of cold, dense gas concentrations in halos with $v_c \geq v_{c,res} = 125, 140, 160 \text{ km s}^{-1}$ ($80, 89, 100 \text{ km s}^{-1}$) at $z = 2, 3, 4$ in the critical density (subcritical) models. Our clearest conclusion is that absorption in halos above these circular velocity thresholds cannot account for the observed incidence $n(z)$ of DLA or LL absorption or for the amount of cold, collapsed gas, Ω_{ccg} , in observed DLA systems, for any of our five cosmological models (Figures 1, 2, 4). Higher resolution simulations are unlikely to change this conclusion, since clumping of the gas on scales below our gravitational softening length would tend to reduce the absorption cross section rather than increase it, unless this small scale clumping could produce neutral condensations in the outskirts of halos where we predict the gas to be mostly ionized. Our models assume $\Omega_b = 0.0125h^{-2}$, and a higher baryon abundance (e.g., Burles & Tytler 1998ab) might increase the predicted absorption. We have investigated SCDM models with different Ω_b values and find that higher Ω_b leads to more absorption per halo as expected, but even a model with $\Omega_b = 0.03125h^{-2} = 0.125$ has too little absorption to match the observations. We will report further results from this study in a future paper.

If any of these cosmological models is correct, then a substantial fraction of high redshift DLA absorption must arise in halos with $v_c \lesssim 100 - 150 \text{ km s}^{-1}$. This conclusion appears consistent with the imaging of DLA fields, which often reveals no large, bright galaxies near the line of sight (Fontana et al. 1996; Le Brun et al. 1997; Moller & Warren 1998; Rao & Turnshek 1998). However, it implies that the asymmetric metal-line profiles found by Prochaska & Wolfe (1997, 1998) must be interpreted as a signature of non-equilibrium dynamics (Haehnelt et al. 1998) rather than smooth rotation.

We find a clear and intuitively sensible relationship between high HI column density absorption and the proximity to galaxies (Figure 3). Damped systems typically lie within 10-15 kpc of the center of a host galaxy at $2 \leq z \leq 4$, while lower column densities near the Lyman limit regime typically occur farther from the host galaxy. All DLA and LL absorption in our simulation occurs within collapsed dark matter halos. If it were to occur outside halos in the

actual Universe, it would have to be on size scales smaller than we resolve.

The stellar mass in our simulation is generally a steep function of time in the redshift range $2 < z < 4$, corresponding to a power law in z (Figure 4). The mass in cold collapsed gas, however, remains relatively fixed, indicating that the rate at which gas is converted into stars is roughly equal to the rate at which new gas cools out of ionized halos and condenses into galaxies. This result is expected if the star formation rate is an increasing function of gas density, as it is in our numerical formulation (KWH).

In our simulations, the halo absorption cross sections $\alpha(v_c, z)$ are determined by complex and competing physical processes. If we consider only halos that contain a single gas concentration, then the absorption cross section actually decreases with increasing circular velocity (solid points in Figures 5-7). However, more massive halos are more likely to contain multiple gas concentrations, with the net effect that $\alpha(v_c, z)$ increases with increasing v_c . At $z = 2$, the models with the weakest mass fluctuations (TCDM and LCDM) tend to have high $\alpha(v_c)$ (Figure 8). This fact, and the trend for single-absorber halos, imply that DLA and LL absorption cross sections are substantially affected by non-equilibrium dynamics: absorbers get smaller if they have time to cool and condense in a quiescent dark matter potential well. This apparent behavior could perhaps be explained as a numerical artifact of overestimating absorption cross sections in systems that are less well resolved, and we will have to examine this point in the future when higher resolution simulations are available. However, we suspect that this non-equilibrium behavior is a real feature of DLA and LL systems, the geometric counterpart to the complex kinematic behavior found by Haehnelt et al. (1998). The physical complexity of $\alpha(v_c, z)$ implies that an accurate fully analytic description of high column density absorption in CDM models will be difficult to achieve. Even the simple expectation that more small scale power produces a higher incidence of DLA and LL absorption does not always hold.

In order to estimate the amount of absorption in halos below the resolution limits of our simulations, we adopted a procedure similar to that of GKHW, using the numerical results to calibrate $\alpha(v_c, z)$ and the Press-Schechter approximation to compute the halo abundance. As in GKHW, our extrapolation of $\alpha(v_c, z)$ below $v_{c,res}$ is guided by the physical expectation that photoionization suppresses gas condensation in halos with $v_c \lesssim 40 \text{ km s}^{-1}$ (QKE; Thoul & Weinberg 1995) and by the results of high resolution SCDM simulations that provide estimates of $\alpha(v_c, z) \approx 50 \text{ km s}^{-1}$. However, relative to GKHW we employed a more conservative estimate of $v_{c,res}$, an improved error estimation procedure based on bootstrap analysis instead of Poisson errors, and a different functional form for the damping cutoff that yields better agreement with the $\alpha(v_c, z)$ results for our LCDM and OCDM simulations, which extend to lower v_c than the SCDM simulation available to GKHW. These changes lead to substantially different $\alpha(v_c, z)$ fits (Figure 8) that greatly increase the predicted amount of absorption in halos with $v_c < v_{c,res}$. Our new results for $n(z)$ in the SCDM model supersede those of GKHW, since our new procedures are certainly an improvement, and our results for $n(z)$ in other models supersede those of GKHW, since in addition to these technical improvements we now have numerical simulations of these other

models to constrain $\alpha(v_c, z)$ for $v_c \geq v_{c,res}$. The bootstrap procedure yields believable statistical uncertainties in the $n(z)$ predictions. The weakest link in our calculations is our reliance on a specified form (equation 3) of $\alpha(v_c, z)$, a product of a power law and the damping function (5). This functional form is only needed to cover a factor $\sim 2 - 3$ range in v_c — from $v_{c,res}$ to the point at 50 km s^{-1} from the high resolution SCDM simulations — but a substantial fraction of the DLA and LL absorption comes from halos in this range.

Taking our results and error estimates at face value, we find that all five of the cosmological models that we consider are compatible with observational estimates of the incidence of DLA and LL absorption at $z = 2, 3$, and 4 , at least at the 2σ level. At the $\sim 1\sigma$ level, the CCDM and SCDM models predict somewhat too much DLA absorption and about the right amount of LL absorption, while the OCDM and LCDM models predict the right amount of DLA absorption and too little LL absorption (especially LCDM). The TCDM model is compatible with the observations, but for the reasons discussed in §4.1 we regard our $z = 3$ and $z = 4$ predictions for this model as upper limits rather than accurate estimates, and we suspect that higher resolution simulations would show it to have too little structure to explain observed high column density absorption at these redshifts.

In the first 3-d hydrodynamic study of high column density absorption, KWHM found that the predictions of $n(z)$ from their simulations of the SCDM model fell a factor of two short of the observed DLA abundance but a factor of ten short of the observed LL abundance. They speculated that the DLA shortfall could be made up by absorption in lower mass halos but that the LL shortfall might imply a distinct physical mechanism for the formation of LL systems, such as thermal instability on mass scales far below the simulation’s resolution limits (Mo & Miralda-Escudé 1996). Our results here support the first speculation but raise the interesting possibility that standard cosmological models can explain the observed LL systems with the physical processes that already occur in these simulations, albeit in halos somewhat below our current resolution limits. Confirmation of this possibility must await simulations that resolve these lower mass halos, but it may be that LL and DLA absorption are closely related rather than physically distinct phenomena, with LL absorption arising preferentially at larger galactocentric distances and in less massive halos.

Our current simulations provide a number of insights into the physics of DLA and LL absorption in halos with $v_c \gtrsim 100 \text{ km s}^{-1}$. Unfortunately, they also imply that robust numerical predictions of the incidence of high-redshift DLA and LL absorption will require simulations that resolve gas dynamics and cooling in halos with $v_c \sim 40 - 100 \text{ km s}^{-1}$, where our analytic modeling predicts a large fraction of the high column density absorption to occur. Simulations that resolve such halos exist (e.g., QKE; Navarro & Steinmetz 1997), but they do not yet model large enough volumes to predict statistical quantities like $n(z)$. Achieving the necessary combination of resolution and volume is challenging but within reach of current computational techniques. Simulations that meet these requirements will also teach us a great deal about the internal structure of more massive DLA and LL systems and about the connection between these

systems and the population of high redshift galaxies.

We thank Eric Linder for useful discussions. This work was supported by NASA Astrophysical Theory Grants NAG5-3922, NAG5-3820, and NAG5-3111, by NASA Long-Term Space Astrophysics Grant NAG5-3525, and by the NSF under grants ASC93-18185, ACI96-19019, and AST-9802568. Gardner was supported under NASA Grant NGT5-50078 for the duration of this work. The simulations were performed at the San Diego Supercomputer Center.

REFERENCES

Bardeen, J., Bond, J.R., Kaiser, N. & Szalay, A.S. 1986, *ApJ*, 304, 15

Barnes, J.E. & Hut, P. 1986, *Nature*, 324, 446

Bi, H.G., & Davidsen, A. 1997, *ApJ*, 479, 523

Burles, S., & Tytler, D. 1998a, *ApJ*, 499, 699

Burles, S., & Tytler, D. 1998b, *ApJ*, 507, 732

Briggs, F.H., Wolfe, A.M., Liszt, H.S., Davis, M.M. & Turner, K.L. 1989, *ApJ*, 341, 650

Cen, R., Miralda-Escudé, J., Ostriker, J.P., & Rauch, M. 1994, *ApJ*, 437, L9.

Croft, R.A.C., Weinberg, D.H., Katz, N., Hernquist, L., 1997, *ApJ*, 488, 532

Davé, R., Hernquist, L., Katz, N., & Weinberg, D.H. 1999, *ApJ*, 511, 521.

Djorgovski, S.G., Pahre, M.A., Bechtold, J., & Elston, R. 1996, *Nature*, 382, 234

Fontana, A., Cristiani, S., D’Odorico, S., Giallongo, E., & Savaglio, S. 1996, *MNRAS*, 279, L27

Gardner, J. P., Katz, N., Hernquist, L., & Weinberg, D. H. 1997, *ApJ*, 484, 31 (GKHW)

Gardner, J. P., Katz, N., Weinberg, D. H., & Hernquist, L. 1997, *ApJ*, 486, 42 (GKWH)

Gingold, R.A. & Monaghan, J.J. 1977, *MNRAS*, 181, 375

Haardt F., & Madau P. 1996, *ApJ*, 461, 20

Haehnelt, M.G., Steinmetz, M., & Rauch, M., 1998, *ApJ*, 497, 647

Hernquist, L. 1987, *ApJS*, 64, 715

Hernquist, L. & Katz, N. 1989, *ApJS*, 70, 419

Hernquist, L., Katz, N., Weinberg, D.H. & Miralda-Escudé, J. 1996, *ApJ*, 457, L51

Hui, L., Gnedin, N., & Zhang, Y. 1997, *ApJ*, 486, 599

Katz, N., Hernquist, L., & Weinberg D.H. 1999, *ApJ* in press.

Katz, N., Weinberg D.H., & Hernquist, L. 1996, *ApJS*, 105, 19 (KWH)

Katz, N., Weinberg D.H., Hernquist, L., & Miralda-Escudé, J. 1996, *ApJ*, 457, L57 (KWHM)

Kauffmann, G. 1996, *MNRAS*, 281, 475

Kauffmann, G., & Charlot, S. 1994, *ApJ*, 430, L97

Kitayama, T., & Suto, Y. 1996, ApJ, 469, 480

Lacey, C., & Cole, S. 1994, MNRAS, 271, 676

Le Brun, V., Bergeron, J., Boisse, P., & Deharveng, J.M. 1997, A&A, 321, 733.

Ledoux, C., Petitjean, P., Bergeron, J., Wampler, E.J., & Srianand, R. 1998, A&A, 337, 51.

Lucy, L. 1977, AJ, 82, 1013

Ma, C. 1996, ApJ, 471, 13

Ma, C. & Bertschinger, E. 1994, ApJ, 434, L5

Ma, C., Bertschinger, E., Hernquist, L., Weinberg, D. H., & Katz, N. 1997, ApJ, 484, L1

Miralda-Escudé, J., Cen, R. Y., Ostriker, J. P., & Rauch, M. 1996, ApJ, 471, 582

Mo, H.J., Jing, Y.P., & White, S.D.M. 1996, MNRAS, 282, 1096

Mo, H. J., & Miralda-Escudé, J. 1996, ApJ, 469, 589

Mo, H.J. & Miralda-Escudé, J. 1994, ApJ, 430, L25

Moller, P. & Warren, S.J. 1998, MNRAS, 299, 661

Navarro, J. F. & Steinmetz, M. 1997, ApJ, 478, 13

Press, W. H., Rybicki, G. B., & Schneider, D. P. 1993, ApJ, 414, 64

Quinn, T.R., Katz, N., & Efstathiou. G.P. 1996 MNRAS, 278, L49 (QKE)

Pei, Y. C., & Fall, S. M. 1995, ApJ, 454, 69

Petitjean, P., Mücke, J.P., & Kates, R. 1995, A&A, 295, L9

Press, W.H., Schechter, P. 1974, ApJ, 187, 425

Prochaska, J.X. & Wolfe, A. M. 1997, ApJ, 487, 73

Prochaska, J. X., & Wolfe, A. M. 1998, ApJ, 507, 113

Rao, S.M, & Turnshek, D.A. 1998, ApJ, 500, 115

Schiano, A. V., Wolfe, A. M., & Chang, C. A. 1990, ApJ, 365, 439

Stadel, J., Katz, N., Weinberg, D.H., & Hernquist, L. 2000, in preparation

Storrie-Lombardi, L.J., Irwin, M.J., & McMahon, R.G. 1996a, MNRAS, 282, 1330

Storrie-Lombardi, L. J., McMahon, R. G., & Irwin, M. J. 1996b, MNRAS, 283, L79

Storrie-Lombardi, L.J., McMahon, R.G., Irwin, M.J., & Hazard, C. 1994, *ApJ*, 427, L13

Thoul, A.A. & Weinberg, D.H. 1996, *ApJ*, 465, 608

Tyson, N. D. 1988, *ApJ*, 329, L57

Weinberg, D.H., Hernquist, L. & Katz, N. 1997, *ApJ*, 477, 8

Wolfe, A.M., Lanzetta, K.M., Foltz, C.B., & Chaffee, F.H. 1995, *ApJ*, 454, 698

Wolfe, A.M., & Prochaska, J.X. 1998, *ApJ*, 494, 15

Wolfe, A.M., Turnshek, Lanzetta, K.M., & Lu, L. 1993, *ApJ*, 385, 151

Zhang, Y., Anninos, P., & Norman, M.L. 1995, *ApJ*, 453, L57

Zhang, Y., Anninos, P., Norman, M.L., & Meiksin, A., 1997, *ApJ*, 485, 496